



저작자표시-비영리-변경금지 2.0 대한민국

이용자는 아래의 조건을 따르는 경우에 한하여 자유롭게

- 이 저작물을 복제, 배포, 전송, 전시, 공연 및 방송할 수 있습니다.

다음과 같은 조건을 따라야 합니다:



저작자표시. 귀하는 원저작자를 표시하여야 합니다.



비영리. 귀하는 이 저작물을 영리 목적으로 이용할 수 없습니다.



변경금지. 귀하는 이 저작물을 개작, 변형 또는 가공할 수 없습니다.

- 귀하는, 이 저작물의 재이용이나 배포의 경우, 이 저작물에 적용된 이용허락조건을 명확하게 나타내어야 합니다.
- 저작권자로부터 별도의 허가를 받으면 이러한 조건들은 적용되지 않습니다.

저작권법에 따른 이용자의 권리는 위의 내용에 의하여 영향을 받지 않습니다.

이것은 [이용허락규약\(Legal Code\)](#)을 이해하기 쉽게 요약한 것입니다.

[Disclaimer](#)

이학박사학위논문

동아시아 지역에서 장기간 지속되는
에어로졸 고농도 사례와 복사효과에
대한 기후학적 이해

Climatic understanding of long-lasting high aerosol
concentration episodes and the radiative effect over East
Asia

2015 년 2 월

서울대학교 대학원

지구환경과학부

오 혜 련

Climatic understanding of long-lasting high aerosol concentration episodes and the radiative effect over East Asia

**By
Hye-Ryun Oh**

Dissertation Submitted to the Faculty of the Graduate School of
the Seoul National University in Partial Fulfillment of the
Requirement for the Degree of Doctor of Philosophy

Degree Awarded:
February 2015

Advisory committee:

Professor	Rokjin Park, Chair	
Professor	Chang-Hoi Ho,	Advisor
Professor	Meehye Lee	
Doctor	Chang-Keun Song	
Professor	Yong-Sang Choi	

이학박사학위논문

동아시아 지역에서 장기간 지속되는
에어로졸 고농도 사례와 복사효과에
대한 기후학적 이해

Climatic understanding of long-lasting high aerosol
concentration episodes and the radiative effect over East
Asia

2015 년 2 월

서울대학교 대학원

지구환경과학부

오 혜 련

동아시아 지역에서 장기간 지속되는 에어로졸
고농도 사례와 복사효과에 대한 기후학적 이해
Climatic understanding of long-lasting high aerosol
concentration episodes and the radiative effect over East
Asia

지도교수 허 창 회

이 논문을 이학박사 학위논문으로 제출함
2014년 10월

서울대학교 대학원
지구환경과학부
오 혜 련

오혜련의 이학박사 학위논문을 인준함
2014년 12월

위 원 장 _____ (인)

부위원장 _____ (인)

위 원 _____ (인)

위 원 _____ (인)

위 원 _____ (인)

ABSTRACT

Climatic understanding of long-lasting high aerosol concentration episodes and the radiative effect over East Asia

Hye-Ryun Oh

School of Earth and Environmental Sciences

The Graduate School

Seoul National University

No other region in the world is as large and diverse a source of aerosols as the Asian continent. In particular, considerable amounts of air pollutants are generated in China, and the effects of trans-boundary transport of diverse aerosols including air pollutants on human health and regional climate are of multilateral concern in East Asia.

Here, we firstly revealed the mechanism of occurrence and transport for the long-lasting high-PM₁₀ episodes for 13 years (2001–2013) in Seoul, Korea and its link with air pollutants originating in China. Our result show that aerosols originating in China play a major role in the occurrence of multi-day (≥ 4 days) severe air pollution episodes in Seoul, Korea, where the concentration of PM₁₀ exceeds 100 $\mu\text{g m}^{-3}$. Observations show that these multi-day severe air quality episodes occur when a strong high-pressure system resides over the eastern China - Korea region. Such a weather condition confines air pollutants within the atmospheric boundary layer and spread them by slow westerlies within the

boundary layer from China into the neighboring countries. These particles lead to air quality deterioration in the short-term perspective, furthermore those result in the change in a radiation properties and an energy budget in the long-term perspective.

Thus, in a climatic sense, we attempted an observationally based estimation of aerosol direct radiative effect (DRE) for all-sky (both clear- and cloudy-sky) over East Asia (80°E–200°E, 20°N–60°N) for May 2000–December 2005. To reliably estimate all-sky DRE of aerosol over East Asia, we used a combining methodology between the measured a clear sky and the simulated DRE for a cloud sky in each 1°-grid. For the measured clear-sky DRE, we employed aerosol, cloud, and radiation fluxes from the Cloud and Earth's Radiant Energy System (CERES) instrument and the Moderate Resolution Imaging Spectroradiometer (MODIS) onboard the Terra satellite. For the simulated cloudy-sky DRE, we performed radiative transfer modeling with the MODIS cloud properties in addition to the aerosol optical properties independently estimated in this study that include asymmetry factor and single scattering albedo. The results show that the global mean \pm standard deviation of DRE for the all-sky scene is $-3.57 \pm 2.3 \text{ W m}^{-2}$, which is weaker than that for the clear-sky only. This implies that DRE of both total and anthropogenic aerosol is considerably diminished by clouds interrupting solar reflection of aerosols. Particularly, for oceanic area of study domain with optically thick and a large amount cloud, the dimming effect by aerosols is amplified, which results in positive aerosol DRE

for all-sky.

Understanding such dynamical processes is a key for advancing the predictability of trans-boundary air pollutants and their health impacts in East Asia as well as developing international measures to improve air quality for the region. And further, evaluation of aerosol DRE for all-sky condition would contribute to reduce the large uncertainty by aerosols over East Asia, which can give some insight to simulate the future climate in model.

Keywords: Aerosol direct radiative effect, All-sky, Cloud, Satellite data, Long-lasting high PM₁₀, Transboundary air pollutant

Student number: 2008-30113

Preface

This thesis includes the following papers:

1. **Oh, H.-R.**, C.-H. Ho, J. Kim, D. Chen, S. Lee, Y.-S. Choi, L.-S. Chang, and C.-K. Song, 2014, Long-range transport of air pollutants originating in China: A possible major cause of multi-day high-PM₁₀ episodes during cold season in Seoul, Korea, *Atmospheric Environment*, (submitted).
2. **Oh, H.-R.**, Y.-S. Choi, C.-H. Ho, and M.-J. Jeong, 2013, Estimation of aerosol direct radiative effects for all-sky conditions from CERES and MODIS observations, *Journal of Atmospheric and Solar-Terrestrial Physics*, 102, 311–320.
3. **Oh, H.-R.**, C.-H. Ho, and Y.-S. Choi, 2013, Comments on “Direct radiative forcing of anthropogenic aerosols over oceans from satellite observation”, *Advances in Atmospheric Science*, 30(1), 10–14, doi: 10.1007/s00376-012-1218-5.
4. Choi, Y.-S., C.-H. Ho, **H.-R. Oh**, R. J. Park, and C.-G. Song, 2009, Estimating bulk optical properties of aerosols over the western North Pacific by using MODIS and CERES measurements, *Atmospheric Environment*, 43, 5654–5660.

TABLE OF CONTENTS

Abstract.....	1
Table of Contents	5
List of Figures	7
List of Tables	11
1. Introduction	12
2. Data and model.....	17
2.1. Satellite observations.....	17
2.2.1. <i>Clouds and the Earth's Radiant Energy System</i>	17
2.2.2. <i>Moderate Resolution Imaging Spectroradiometer</i>	19
2.2.3. <i>Cloud-Aerosol Lidar with Orthogonal Polarization</i>	21
2.2. Ground-based observations.....	23
2.2.1. <i>Aerosol Robotic Network</i>	23
2.2.2. <i>Particulate matter with a diameter $< 10 \mu\text{m}$ (PM_{10})</i>	24
2.3. Reanalysis data.....	26
2.3.1. <i>NCEP-NCAR reanalysis data II</i>	26
2.4. Radiative transfer model.....	27
2.4.1. <i>Santa Barbara DISORT Atmospheric Radiative Transfer Model (SBDART)</i>	27
3. Methodology	29
3.1. Definition of aerosol direct radiative effect for clear- and all-sky.....	29
3.1.1. <i>Aerosol direct radiative effect for clear-sky</i>	29
3.1.2 <i>Aerosol direct radiative effect for all-sky</i>	31
3.2 Estimating aerosol optical properties	33
3.2.1. <i>Retrieval of aerosol single scattering albedo and aerosol asymmetry factor</i>	33
3.3. Estimating aerosol direct radiative effect for all-sky	38
3.3.1. <i>Direct radiative effect of total aerosol for all-sky</i>	38
3.3.2 <i>Direct radiative effect of anthropogenic aerosol for all-sky</i>	46
4. Occurrence and transport mechanism for lasting-day of high PM_{10} episodes in	

Seoul	48
4.1. High-PM ₁₀ days during 2001–2013:	48
4.1.1 1-day episode vs. multi-day episode.....	48
4.2. Trans-boundary transport of PM ₁₀ from China to Seoul.....	53
4.2.1 Atmospheric circulation field	53
4.2.2 Station observations and backtrjectory analysis	60
4.2.3 Satellite observed aerosol vertical profile.....	65
4.3. Summary and discussion	68
5. Estimated radiative impact of aerosols for clear- and all-sky	72
5.1. Influencing factors on aerosol radiative effect.....	72
5.1.1 Aerosol optical depth, aerosol single scattering albedo and aerosol asymmetry factor	72
5.1.2. Cloud fration, cloud top temperature, cloud effective radius, and cloud optical depth.....	81
5.1.3 Aerosol vertical profile and its frequency above cloud from the CALIOP observation	84
5.2. Direct radiative effect of total and anthropogenic aerosols	90
5.2.1 Direct radiative effect of total aerosol	90
5.2.2 Direct radiative effect of anthropogenic aerosol	96
5.2.3 Validation and assesement of its uncertainty	101
5.3. Summary and discussions.....	108
6. General conclusions.....	112
Reference	115
국문초록	115

LIST OF FIGURES

Figure 1.1. Aerosol optical depth from the MODIS during 2000–2005 (a) and dominant aerosol type (b) in in a given $10^\circ \times 10^\circ$ grid from the CALIOP-observation during 2007–2010.....	15
Figure 1.2. Percentage of six aerosol types over East Asia (a) and globe (b) from the CALIOP-observation during 2007–2010.....	16
Figure 3.1. Flowchart to estimate the single scattering albedo (ASSA) and asymmetry factor (AAF) based on the CERES observation and radiative transfer model.	36
Figure 3.2. Simulated aerosol direct radiative effect in terms of aerosol optical depth for various ω and g at the TOA (a and b) and the surface (c and d). The shaded area denotes the existent range in observations.....	37
Figure 3.3. Flowchart for the methodology of estimating ΔDRE	44
Figure 3.4. Simulated ΔDRE against COD for various ER, ST minus CTT and surface albedo for (a) ASSA = 0.87 and AAF = 0.52 and for (b) ASSA = 0.99 and AAF = 0.76. Black and grey lines denote surface albedos of 0.1 and 0.3, respectively.	45
Figure 4.1. Annually averaged PM_{10} concentration (\circ), days of high- PM_{10} concentration episodes ($\geq 100 \mu g m^{-3} day^{-1}$) from 27 air quality monitoring stations in Seoul. Black and grey bars denote the multi-day (≥ 4 days) and 1-day episodes in each year, respectively.....	51

Figure 4.2. The number of high-PM ₁₀ concentration days in each season. Black and grey bars denote multi-day and 1-day episodes, respectively.	52
Figure 4.3. Composite of anomalous geopotential height (a and e), vertical wind (b and f), zonal wind (c and g), and meridional wind (d and h) at 37.5°N as functions of longitude and pressure on the onset day of multi-day (upper panel) and 1-day (lower panel) high-PM ₁₀ concentration episodes.	57
Figure 4.4. Composite of anomalous geopotential height and wind vector at 1000 hPa (a and c) and 850 hPa (b and d) on the onset day of multi-day (upper panel) and 1-day (lower panel) high-PM ₁₀ concentration episodes. Shading denotes the regions significant at the 99% confidence level based on a t-test.	58
Figure 4.5. Same as Supplementary Fig. 4.4, except for –2 day high-PM ₁₀ concentration episodes.	59
Figure 4.6. Spatial distribution (a and b) of anomalous PM ₁₀ concentrations measured from each of the 73 sites on –1 day of each high-PM ₁₀ episode, and 72-h wind back trajectory in cold (October–March; blue lines) and warm (April–September; red lines) seasons from the HYSPLIT model (a, c and d, d). The circle size in each figure denotes the anomalous PM ₁₀ concentration against monthly climatology, respectively. The stations in 1 and 2 in Figs. 4.6a and 4.6d are Beijing and Tianjin, respectively. Each closed circle is a 24 h interval in Figs. 4.6c and 4.6d.	63

Figure 4.7. Spatial distribution of anomalous PM_{10} concentrations measured from each of the 73 sites on –2 day and –3 day of multi-day (a and b) and 1-day (c and d) high- PM_{10} episodes.....	64
Figure 4.8. Vertical profile of aerosol pixel number for high- PM_{10} concentration episodes from the CALIOP. Each line denotes a collocated case around Seoul for multi-day (a) and 1-day (b) episodes.....	67
Figure 4.9. Schematic diagram of multi-day high- PM_{10} episodes in Seoul, Korea.	71
Figure 5.1. MODIS-observed annual-mean aerosol optical depth (a), and fine mode fraction (b) over East Asia ($80^{\circ}E$ – $200^{\circ}E$, $20^{\circ}N$ – $60^{\circ}N$).....	78
Figure 5.2. Spatial distribution of anthropogenic aerosol optical depth by the method suggested from Kaufman et al. (2005) over East Asia ($80^{\circ}E$ – $200^{\circ}E$, $20^{\circ}N$ – $60^{\circ}N$).	79
Figure 5.3. Spatial distributions of the estimated the annual average of (a) ASSA and (b) AAF over East Asia ($80^{\circ}E$ – $200^{\circ}E$, $20^{\circ}N$ – $60^{\circ}N$).....	80
Figure 5.4. MODIS-observed annual-mean (a) cloud fraction (%), (b) CTT (K), (c) ER (μm) and (d) COD during year 2000–2005. The annual-mean is monthly averages of daily data for entire periods.....	83
Figure 5.5. Annual-averaged vertical distribution of anthropogenic aerosols (a) and total aerosols for the period of 2007–2010 from the CALIOP.....	88
Figure 5.6. (a) Four aerosol vertical profiles and cloud layer at 2 km altitude (blue area) as the conditions of RTM experiments and (b) the simulated ΔDRE	

against COD for the different profiles. The ratio in x-axis indicates the value for the number of aerosol in each layer divided by the maximum number of aerosol in a layer among the all layers.....	89
Figure 5.7. Spatial distributions of the annual-averaged (a) aerosol DRE _{clear} , (b) Δ DRE (c) aerosol DRE _{all}	94
Figure 5.8. Monthly variations in the aerosol DRE _{clear} and aerosol DRE _{all} over the nine regions. The closed and open circles denote the aerosol DRE _{clear} and DRE _{all} , respectively. The nine regions are denoted as follow; Mediterranean basin (a), India (b), East Asia (c), West coast of U.S.A. (d), East coast of U.S.A. (e), West coast of North Africa (f), Australia (g), Amazon basin (h) and Southern hemisphere ocean (i).....	95
Figure 5.9. Global distribution of anthropogenic aerosol radiative forcing (ARF) for all-sky by Chen et al. (2011) (ARF _{1all} ; a–d) and the present study (ARF _{2all} ; e–h) and their difference (i–l) for four seasons of the year 2005.....	100
Figure 5.10. Dependency in the Δ DRE as a function of the COD for (a) south east China (100°E–130°E, 20°N–45°N), (b) India (70°E–95°E, 10°N–30°N) and (c) Africa (5°W–30°W, 10°N–30°N) from the CERES-observation and RT model. The box plots are the CERES observations, which sum up the distribution, median and variability in the Δ DRE corresponding to the COD. The solid circles are the Δ DRE simulated by the RT model over each region.	107
Figure 5.11. Summary of aerosol radiative effect for clear-sky (a) and all-sky (b) over East Asia.	100

LIST OF TABLES

Table 3.1. Regression coefficients for estimating ΔDRE as a function of the cloud optical depth (COD), effective radius (ER), and surface temperature (ST) – cloud top temperature (CTT) for four pairs of (ASSA, AAF). Each value for (ASSA, AAF) at $0.63\ \mu m$ is (0.87, 0.52), (0.99, 0.52), (0.87, 0.76), and (0.99, 0.76).....	43
Table 5.1. Comparison of AERONET observations versus the estimations of single scattering albedo and asymmetry factor at Gosan (a), Osaka (b), Anmyon (c), and Taiwan (d). The standard error of the mean is also given.....	77
Table 5.2. Frequency (%) for aerosol above cloud from the CALIOP VFM data for four years (2007–2010).....	87
Table 5.3. Regionally and globally averaged aerosol optical depth for total aerosols (AOD) and anthropogenic aerosols (AODanth), aerosol radiative forcing for all-sky by Chen et al. (2011) (ARF_1^{all}), and the present study (ARF_2^{all}) for four seasons of the year 2005	99
Table 5.4. ΔDRE as a function of global COD from CERES observation (box plots) and RT model (solid circles). The box plots sum up the distribution, median, and variability of ΔDRE	105
Table 5.5. Error source in aerosol DRE for all-sky and its uncertainty.....	106

1. INTRODUCTION

Air quality deterioration by rapid industrialization and urbanization in many regions of the world is directly associated with several social, economic and climatic issues (*Annez and Buckley* 2009; *Yasunari et al.*, 2013, *IPCC*, 2007). Continuous exposure of people to high levels of air pollutants for a long time has become a serious public health hazard, which causes an increase in cardiac and respiratory morbidity and mortality (*Chen and Kan*, 2008; *Fajersztajn et al.*, 2013). Moreover, massive and diverse aerosols including air pollutants in atmosphere is directly involved in earth energy budget and hydrologic cycle, which can influence on a regional climate change (*Ramanathan et al.*, 2001; *Kaufman et al.*, 2005; *IPCC*, 2007).

Particularly, East Asia where industrial activities have explosively grown over recent decades is notorious for bad air quality (*Chan and Yao*, 2008; *Fang et al.*, 2009). For China, although the annual-mean PM_{10} (particulate matter with diameters $\leq 10 \mu\text{m}$) concentration decreased slightly from $120 \mu\text{g m}^{-3}$ in 2003 to $100 \mu\text{g m}^{-3}$ in 2009, the PM_{10} value is still very high, reaching at approximately five times of criteria (i.e., $20 \mu\text{g m}^{-3}$ per year) suggested by the World Health Organization (WHO) (*Zhu et al.*, 2011). It means that the large and diverse aerosols always float in the region (Fig. 1.1, Fig. 1.2), which causes a change in aerosol direct radiative effect (DRE) by enforced scattering and absorption of solar energy: aerosol DRE for clear-sky (i.e., cloud-free) is about two to four

times greater than global averaged DRE (i.e., $-4.9 \pm 0.7 \text{ W m}^{-2}$ over the land) at the top-of-atmosphere (TOA) (Yu *et al.*, 2006; Zhao *et al.*, 2011).

More troubling is the fact that air quality problems are not only confined to China but also affect the immediate downwind regions, including Korea and Japan, and sometimes as far as the western North American region across the Pacific Ocean (Heo *et al.*, 2009; Fu *et al.*, 2011; Lin *et al.*, 2014). For instance, on January 12, 2013, the hourly averaged PM concentration in urban areas of central and eastern China were over $700 \mu\text{g m}^{-3}$, with the extreme levels reaching up to $900 \mu\text{g m}^{-3}$ (<http://cleanairinitiative.org/portal/node/11599>) and continuing for approximately one week (Wang *et al.*, 2013; Park *et al.*, 2013). At the same time, Seoul (and some parts of Japan) experienced consecutive days with the PM_{10} level $\geq 100 \mu\text{g m}^{-3}$ from 12 to 15 (from 13 to 15) January 2013. The long-lasting high- PM_{10} episode resulted in an abnormally large number of respiratory admissions and caused traffic congestion and flight cancellations. It is strongly suspected that large amounts of air pollutants emitted in China are directly related to high- PM_{10} episodes in Seoul and parts of Japan.

For the reason, numerous attempts have been accomplished to reveal the cause of occurrence and transport mechanism for highly polluted episode for several days and further quantify climatic impact in East Asia (Lee *et al.*, 2013; Wang *et al.*, 2014; Zheng *et al.*, 2014). However, these most studies have examined only one or few high pollution episode over short periods. Besides they have been confined only for clear-sky scenes due to difficulty in removing

contribution by cloud from all-sky (i.e., both clear-sky and cloudy-sky) radiation (Yu *et al.*, 2006; Li *et al.*, 2010). Considering the fact that the cloud coverage in East Asia is over 60% (Myhre *et al.*, 2009; Kay *et al.*, 2012) and an enormous amount of aerosols is overlapped with clouds (Devasthale and Thomas, 2011), the estimation of aerosol DRE for all-sky could result in significant change of the DRE magnitude for clear-sky.

Therefore, the main scientific objectives of this thesis are summarized as the following:

- (1) To reveal the mechanism of occurrence and transport for the multi-day (\geq 4 days) high-PM₁₀ episodes in Seoul, Korea and its link with air pollutants originating in China.
- (2) To diagnosis and assessment of climatic radiative impact of total and anthropogenic aerosol for all-sky over East Asia.

This dissertation is organized as follows:

Chapter 2 describes the various observational data and radiative transfer model used. The detail methodology to estimate all-sky DRE is given in Chapter 3. A possible major cause of multi-day high-PM₁₀ episodes in Seoul is investigated in Chapter 4, and the estimated climatic aerosol DRE over East Asia is presented in Chapter 5. Finally, Chapter 6 summarizes the findings of the study.

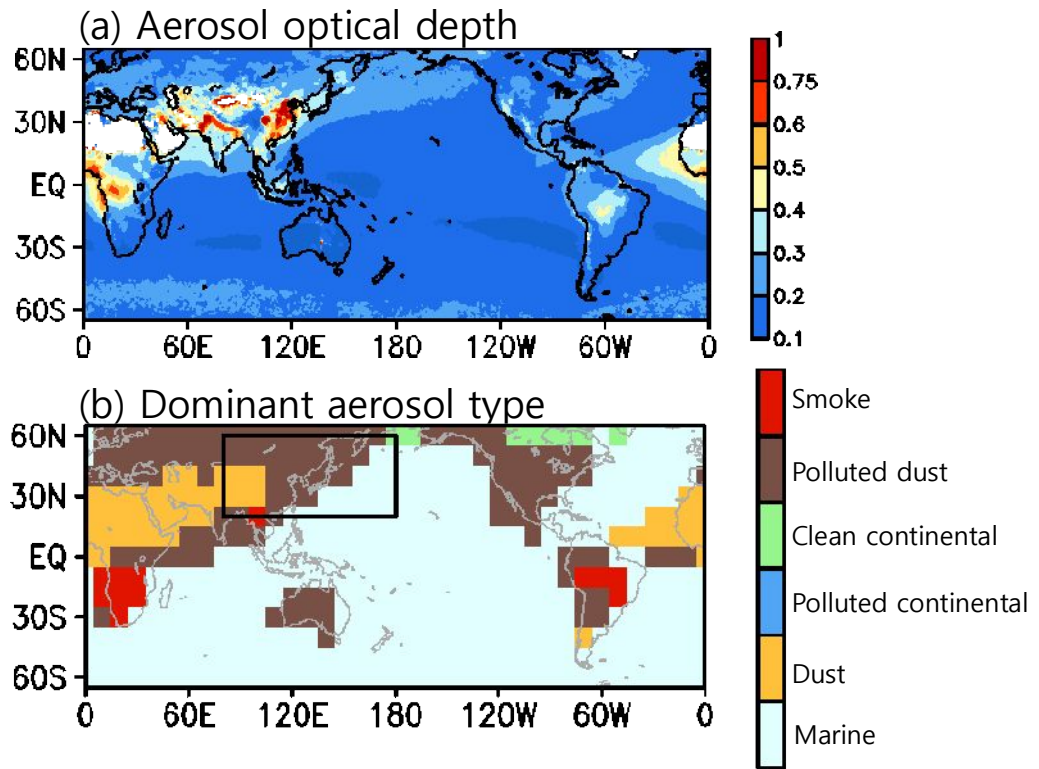
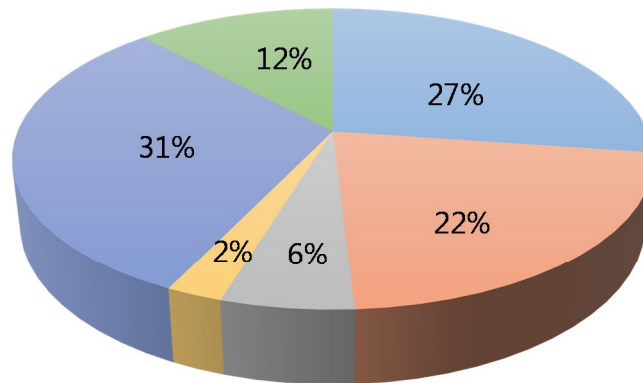


Figure 1.1. Aerosol optical depth from the MODIS during 2000–2005 (a) and dominant aerosol type (b) in in a given $10^\circ \times 10^\circ$ grid from the CALIOP-observation during 2007–2010.

(a) East China



(b) Globe

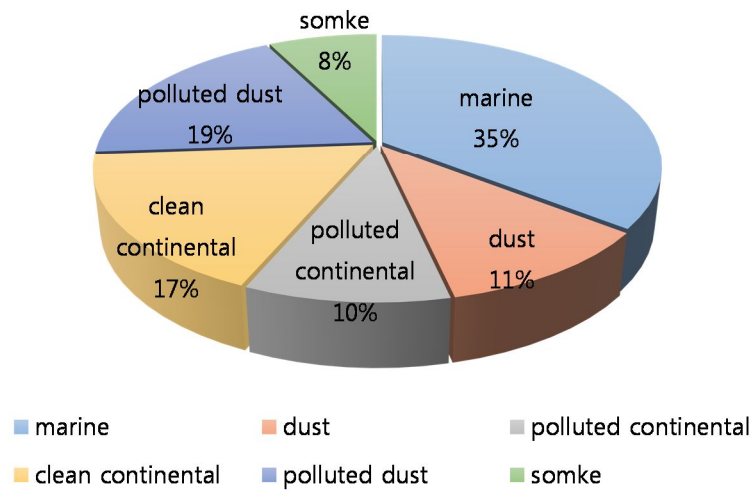


Figure 1.2. Percentage of six aerosol types over East Asia (a) and globe (b) from the CALIOP-observation during 2007–2010.

2. DATA AND MODEL

2.1. Satellite observations

2.2.1. Clouds and the Earth's Radiant Energy System

In the study, data during May 2000–December 2005 is used for estimating aerosol DRE for all-sky. For consistency, we did not take the data from 2006 when the version of the CERES data was changed. The domain was confined to 60°S–60°N since the satellite aerosol data contain relatively large uncertainty in high latitudes ($> 60^\circ$) due to large surface albedo.

Shortwave flux data at the TOA and surface were taken from the CERES Monthly Gridded Radiative Fluxes and Clouds (FSW, edition 2C). These radiation fluxes available for pristine (without clouds and aerosols), clear-sky (without clouds and with aerosols) and cloudy-sky (with clouds and aerosols) conditions were averaged over a $1^\circ \times 1^\circ$ latitude-longitude grid. The flux for pristine condition cannot be observed, so it is computed by radiative transfer calculations (*Charlock et al.*, 2005). The clear-sky condition is defined as the cases with cloud amounts of less than 0.1% in footprints of a 20 km nadir-resolution. The bias in the instantaneous shortwave flux at the TOA is known to be 2–5% and 4–6% for clear-sky and cloudy-sky conditions, respectively (http://eosweb.larc.nasa.gov/PRODOCS/ceres/SSF/Quality_Summaries/ssf_toa_terra_ed2B.html).

Along with the shortwave fluxes at the TOA and surface, the information of aerosol optical depth (AOD) at 0.63 μm , surface albedo, and cloud products in the CERES FSW was used. These data were basically obtained from MODIS, and then collocated inside the CERES flux footprints to give consistency between the shortwave flux and each product. If MODIS AOD is not available for the footprint with cloudiness more than 50% or deserts, AOD is made from the National Center for Atmospheric Research (NCAR) Model for Atmospheric Transport and Chemistry (MATCH) (http://eosweb.larc.nasa.gov/PRODOCS/ceres/CRS/Quality_Summaries/CER_CRSTerra_Edition2B.html). The surface albedo was estimated from MODIS imager pixels, pre-calculated lookup tables and RTM developed by Fu and Liou RTM (*Fu and Liou*, 1993), which is approximately 0.02 lower than that of the ground observation due to a different spatial resolution (*Rutan et al.*, 2009). The cloud products are divided into four pressure layers (e.g., high, upper middle, lower middle, and low). For a single layer cloud within the footprint, it is defined as the lower layer regardless of its height while for a multi-layer cloud it corresponds to the CTT. In the study, we concentrate on the single layer cloud and we thereby use CTT, CF, ER, and COD in the low level.

2.2.2. Moderate Resolution Imaging Spectroradiometer

To guarantee consistency with CERES data, we analyzed spatial distributions of aerosol and cloud properties during 6 years (2000–2005) obtained from the MODIS/Terra Level-3 daily gridded atmospheric data product (MOD08, collection 5). The latitude-longitude spatial resolution of the MOD08 data is $1^\circ \times 1^\circ$.

For aerosol properties, we use aerosol optical depth (AOD), fine mode fraction (FMF) data. The MODIS algorithm retrieves AOD for this wavelength by interpolating the values at 470 and 660 nm (*Remer et al.*, 2005). The uncertainty of the MODIS AOD data over the ocean and land is known to be $\pm 0.03 \pm 0.05 \times \text{AOD}$ and $\pm 0.05 \pm 0.15 \times \text{AOD}$, respectively (*Levy et al.*, 2003; *Remer et al.*, 2002; *Remer et al.*, 2005). The MODIS FMF value also indicates the size distribution of aerosols, defined as the ratio of the contribution of the fine-mode AOD (i.e., with an effective aerosol radius less than $1 \mu\text{m}$) to the total AOD. On average, the MODIS FMF value is often higher than that from airborne measurements, because the MODIS algorithm assumes that the aerosols are spherical (*Levy et al.*, 2003; *Anderson et al.*, 2005).

For cloud properties, cloud fraction, cloud top temperature (CTT), cloud optical depth (COD), and cloud effective radius (ER) were used. The cloud fraction is produced by using a cloud mask obtained from various threshold tests of spectral reflectance and brightness temperature (*King et al.*, 1997; *Platnick et al.*, 2003). A main error source of cloud fraction results from cloud mask that has

an uncertainty of 15% (*Ackerman et al.*, 2008). The CTT developed by *Menzel et al.* (1983) was converted from the cloud top pressure retrieved using a CO₂ slicing technique with CO₂ absorption channels within 13.2–14.4 μm . The uncertainty of CTT is less than 1 K considering error due to MODIS 10.8 μm calibration and humidity profile (*Dong et al.*, 2008). The total-column COD and ER were determined using a combination of visible and near-IR channels (*King et al.*, 1997). *Dong et al.* (2008) reported that the uncertainty of COD and ER retrieved from the MODIS is 8% and 15%, respectively.

2.2.3. Cloud-Aerosol Lidar with Orthogonal Polarization

To calculate an uncertainty subject to aerosol vertical profile in the aerosol DRE for all-sky, we additionally used the Cloud-Aerosol Lidar with Orthogonal Polarization (CALIOP) level-2 vertical feature mask (VFM) (*Winker et al.*, 2007) data. Since the data is available after May 2006, we analyzed the aerosol type and cloud profiles for four years (January 2007–December 2010). CALIOP's laser transmits linearly polarized light simultaneously at 532 nm and 1064 nm at a pulse rate of 20.16 Hz, and its receiver measures backscatter intensity at two wavelength, with the latter divided into two orthogonally polarized components. Thus this instrument observes both cloud and aerosols at high spatial resolution. Generally, the aerosol vertical profile when remotely sensed from the ground is expressed as an extinction coefficient, that is, the fraction of light lost to scattering and absorption by aerosol particles as a function of altitude. The aerosol extinction coefficient at surface level can be derived from the visibility. Since the integrated extinction coefficient over a vertical column of unit cross section corresponds to AOD, the aerosol extinction coefficient at each altitude can be calculated using a known AOD value and aerosol scaling height. The aerosol scaling height is a measure of the decrease of aerosol loadings over an altitude, and can be estimated from the surface visibility and AOD value.

The aerosol algorithm in the CALIOP is based on the cluster analysis of the Aerosol Robotic Network (AERONET) (1993–2002) data to determine extinction-to-backscatter ratio for each aerosol type (*Omar et al.*, 2009). The

cluster is classified into six aerosol types (e.g., desert dust, smoke, clean continental, polluted continental, marine, and polluted dust) allowing for an uncertainty of 30% of extinction-to-backscatter ratio (*Omar et al.*, 2009). Cloud is detected by the layer-integrated particle depolarization ratio at 532 nm, and the cloud-top and cloud-bottom temperatures (*Hu et al.*, 2009). The cloud mask is in agreement with that for MODIS in more than 85% on a global scale (*Holz et al.*, 2008). Confidence level of Aerosol and cloud pixel detected in CALIOP is determined by the Cloud Aerosol Discrimination (CAD) algorithm: the probability distribution functions of the altitude-and-latitude-dependent feature integrated color ratio, layer-integrated volume depolarization ratio, and attenuated backscatter coefficient in 532 nm³⁰. Accordingly, a CAD score between -100 (0) and 0 (100) denotes aerosol (cloud), which is used to give the confidence level. Thus, we only used aerosol pixels with a medium ($50 \leq |\text{CAD score}| < 70$) or high ($|\text{CAD score}| \geq 70$) confidence score to minimize the effect of misclassification between aerosol and cloud. The horizontal and vertical resolutions of the data are 333 m and 30 m below 8.2 km and those are 1000 m and 60 m from 8.2 km to 20.2 km, respectively.

2.2. Ground-based observations

2.2.1. Aerosol Robotic Network

To validate the independently retrieved ASSA and AAF values estimated in this thesis, we used the ground-based observations of the two values at 675 nm from Aerosol Robotic Network (AERONET) sites. The uncertainty of the AERONET ASSA and AAF is known to be from ± 0.01 to ± 0.03 and from ± 0.03 to ± 0.08 , respectively, for all types of aerosols (*Zhou et al.*, 2005). We selected four AERONET sites that are adjacent to the ocean and that provide consecutive data for the period of analysis: Gosan (126°E, 33°N), Osaka (135°E, 34°N), Anmyon (126°E, 36°N), and Taiwan (121°E, 25°N). These stations are all located in the coastal sea area defined in this study. The AERONET level-2 data were obtained during a successful Terra overpass from 1000 through 1200 hours local time (LT). We then compared the station averages with the 1°-grid averages of the daily estimates. However, because of the limited number of samples from each station, it is currently impossible to validate the daily estimates

2.2.2. Particulate matter with a diameter $< 10 \mu\text{m}$ (PM_{10})

We used hourly PM_{10} mass concentration data for 2001–2013 over 27 air quality monitoring stations in Seoul. To minimize the local effect, we excluded stations that included high fluctuations of PM_{10} due to emissions from local vehicles and industrial plants. PM_{10} concentration is measured by the increase in attenuation when beta rays irradiate particulate matter collected on a filter, and is referred to as the beta-ray absorption method²⁶. The bias in the measuring method is known to be approximately 10%, which is mainly due to particle-containing moisture. The recorded hourly data is then accumulated to obtain the daily average.

To support the possibility of inflow of China-originated air pollutants to Seoul, we further analyzed the PM_{10} concentration in China and 72-hour back trajectories. Since 2000, China has reported a daily averaged air pollution index (API) in terms of air quality monitoring in many cities. A value for the API can be converted to a mass concentration of PM_{10} using the following equation:

$$\text{PM}_{10} = \left[\frac{\text{API} - \text{API}_{\text{low}}}{\text{API}_{\text{high}} - \text{API}_{\text{low}}} \right] \times (\text{PM}_{10 \text{ high}} - \text{PM}_{10 \text{ low}}) + \text{PM}_{10 \text{ low}}.$$

where API_{high} and API_{low} are the upper and lower standard indices, respectively; and $\text{PM}_{10 \text{ high}}$ and $\text{PM}_{10 \text{ low}}$ are the PM_{10} mass concentrations corresponding to API_{high} and API_{low} , respectively. For example, $\text{PM}_{10 \text{ high}} = 150$

and $PM_{10\text{ low}} = 50$, when $API_{\text{high}} = 100$ and $API_{\text{low}} = 50$, $PM_{10\text{ high}} = 420$ and $PM_{10\text{ low}} = 350$, when $API_{\text{high}} = 300$ and $API_{\text{low}} = 200$. The each upper and lower limits of API and a detailed calculation of PM_{10} concentration are given in Zhang et al. (2003) and Qu et al. (2010). The uncertainty of daily PM_{10} measurements is less than 1%. In this study, PM_{10} concentrations converted from the API are used over 73 stations in China during January 2001–March 2012.

2.3. Reanalysis data

2.3.1. NCEP-NCAR reanalysis data II

In order to investigate the potential pollution source and its trans-boundary transport, daily meteorological data (e.g., geopotential height and the three-dimensional velocity) in Seoul was obtained from the National Centers for Environmental Prediction-National Center for Atmospheric Research (NCEP-NCAR) reanalysis 2, for the same period as PM₁₀ concentrations in Seoul. The data have a horizontal resolution of $2.5^{\circ} \times 2.5^{\circ}$ longitude-latitude, and in the vertical data are distributed on 17 pressure levels ranging from 1000 hPa to 10 hPa (*Kalnay et al.*, 1996).

2.4. Radiative transfer model

2.4.1. Santa Barbara DISORT Atmospheric Radiative Transfer Model (SBDART)

This thesis uses the Santa Barbara DISORT Atmospheric Radiative Transfer (SBDART) developed by *Ricciazzi et al.* (1998) to improve on the LOWTRAN (*Kneizys et al., 1983*) – MODTRAN (*Berk et al., 1983*) codes. A characteristic of the model is that the atmosphere is composed of a discrete number of adjacent homogeneous layers. So, The SSA and optical thickness of aerosol and cloud are constant within each layer. The SBDART provides six standard atmospheric profiles and standard vertical profiles of pressure, temperature water vapor, and ozone density. In addition, SBDART can quantitatively compute the radiative effects of several lower- (i.e., rural, urban, or maritime condition) and upper-atmosphere aerosol types (*Shettle and Fenn, 1975*). The spectral resolutions of the models are 20 cm^{-1} bandwidth in Both SW and LW. The SBDART is known to fairly accurately simulate radiation at all shortwave wavelength; therefore, it has been used for many research purposes in remote sensing of the atmosphere (e.g., *Valero et al., 2003; Choi et al., 2007*). *Valero et al.* (2003) showed a good agreement between the calculated fluxes for clear- and cloudy-sky from the SBDART model to observed fluxes from the ground measurements.

In the study, SBDART is performed to simulate shortwave flues for clear- and all-sky condition respect to the given ASSA and AAF, and cloud properties. The integrated spectral range was set to $0.3\text{--}5.0 \text{ }\mu\text{m}$ and the central wavelength to

0.63 μm , which were equivalent to those of the CERES spectrometer. The prescribed shortwave insolation in the SBDART model was scaled to be comparable with the monthly observations of the solar insolation in the FSW data.

3. METHODOLOGY

3.1. Definition of aerosol direct radiative effect for clear-and all-sky

3.1.1. Aerosol direct radiative effect for clear-sky

To assess the aerosol influence on radiative flux, it is important to consider both quantitative and qualitative effect of aerosol. At first, quantitatively there is direct radiative effect (DRE) of aerosol at some level, which is the change in net radiative flux and it either at the TOA and surface is defined as follows:

$$\text{DRE}_{\text{satellite,TOA(S)}}^{\text{clear}} = F^{\text{NA}} - F^{\text{A}} \quad (1)$$

Where, $\text{DRE}_{\text{satellite,TOA(S)}}^{\text{clear}}$ is the satellite-measured average aerosol DRE at the TOA (surface) for clear-sky scene, and F^{A} and F^{NA} are the shortwave fluxes with and without aerosols respectively.

Secondly, we consider qualitatively the radiative effect because the aerosol impact on radiation significantly differs from its chemical composition, which refers to the DRE efficiency either at the TOA and surface is defined as follows:

$$\text{DRE}_{\text{satellite,TOA(S)}}^{\text{clear}} \text{ efficiency} = \frac{\text{DRE}_{\text{TOA,S}}}{\text{AOD}} \quad (2)$$

Where, AOD is aerosol optical depth.

The DRE efficiency normalized by its column integrated AOD is mainly governed by aerosol size distribution and chemical composition. Therefore the quantity of DRE efficiency depends on aerosol ASSA and AAF and it is less

variable than aerosol DRE. Therefore DRE efficiency is proper to judge aerosol source and is used to retrieve ASSA and AAF, later.

3.1.2 Aerosol direct radiative effect for all-sky

A $1^\circ \times 1^\circ$ domain with fractional cloud coverage η and a clear-sky region with fractional coverage $1-\eta$ are considered. Recall that the aerosol DRE for the cloudy-sky scene cannot be measured by satellite instruments, while that for the clear-sky scene can be measured. Thus the aerosol DRE averaged over all-sky scenes can be derived by the following equation:

$$\text{DRE}^{\text{all}} = \text{DRE}_{\text{satellite}}^{\text{clear}} \times (1 - \eta) + \text{DRE}_{\text{RTM}}^{\text{cloud}} \times \eta, \quad (3)$$

where $\text{DRE}_{\text{satellite}}^{\text{clear}}$ is the satellite-measured average aerosol DRE for clear-sky scene and $\text{DRE}_{\text{RTM}}^{\text{cloud}}$ is the RTM-simulated average aerosol DRE for the cloudy-sky scene. $\text{DRE}_{\text{satellite}}^{\text{clear}}$ is immediately obtained as the difference in the net irradiances with and without the aerosol by using TOA shortwave fluxes from the CERES. We assume that the optical properties of aerosols below clouds are equal to those for the clear-sky in a given $1^\circ \times 1^\circ$ grid. Under this assumption, the aerosol DRE over fractional coverage η is expressed by the summation of aerosol $\text{DRE}_{\text{satellite}}^{\text{clear}}$ and the simulated effect of clouds on aerosol DRE (ΔDRE). Therefore, Eq. (3) becomes:

$$\text{DRE}^{\text{all}} = \text{DRE}_{\text{satellite}}^{\text{clear}} \times (1 - \eta) + (\text{DRE}_{\text{satellite}}^{\text{clear}} + \Delta\text{DRE}) \times \eta. \quad (4)$$

Note that the $DRE_{\text{satellite}}^{\text{clear}}$ is only available for the cloud coverage of $\eta \neq 1$; For $\eta = 1$, DRE^{all} is equal to $DRE_{\text{RTM}}^{\text{cloud}}$. However, there was no case of $\eta = 1$ in the monthly mean. Accordingly, Eq. (4) may be inappropriate for large values of η in a 1° grid. Then Eq. (4) can be arranged as a simpler formula:

$$DRE^{\text{all}} = DRE_{\text{satellite}}^{\text{clear}} + \Delta DRE \times \eta \quad (\eta \neq 1). \quad (5)$$

To derive aerosol DRE^{all} in Eq. (5), the independent calculation of ΔDRE is required. Since, ΔDRE cannot be directly observed, we will introduce a methodology to estimate ΔDRE given in various aerosol and cloud properties, and an obtained relationship between ΔDRE and each parameters in next section.

3.2 Estimating aerosol optical properties

3.2.1. Retrieval of aerosol single scattering albedo and aerosol asymmetry factor

ASSA and AAF are essential parameters to estimate aerosol DRE for both clear- and all-sky. However, the factors are not given in all grid points to estimate global aerosol DRE. Therefore, we independently estimate from the CERES fluxes and AOD.

The flowchart to estimate aerosol intensive properties ASSA and AAF is given in Fig.3.1. The aerosol DRE efficiency at the two layers, TOA and surface, are needed to obtain these properties:

$$\text{DRE}_{\text{satellite,TOA}}^{\text{clear}} \text{ efficiency} = f(\text{ASSA}_{640}, \text{AAF}_{640}) \quad (6)$$

$$\text{DRE}_{\text{satellite,S}}^{\text{clear}} \text{ efficiency} = f(\text{ASSA}_{640}, \text{AAF}_{640})$$

Where, the inferior 640 indicates the wavelength of 640 nm.

The $\text{DRE}_{\text{satellite,TOA(S)}}^{\text{clear}}$ efficiency is expressed by a function of ASSA and AAF in the Eq. 6, which is calculated by using aerosol DRE at TOA and surface and AOD_{640} obtained from CERES observation. RT models were used to quantitatively examine the effects of ASSA and AAF on DRE efficiency. These simulations are helpful in understanding the analytical relationships among aerosol DRE, AOD, ASSA, and AAF.

The results of the simulation are plotted in Fig. 3.2. Note the linear correspondence between AOD and DRE both two layers, regardless of the change in optical properties; therefore, DRE efficiency can be safely defined as the slope of the line. Because they are equivalent to the FSW parameters, we simulated the clear-sky shortwave fluxes for the integrated spectral range (0.3–5.0 μm), and simulated the aerosol optical properties for the wavelength 630 nm, respectively. We scaled the assumed shortwave insolation in the SBDART model to conform to day-to-day observations of solar insolation in the FSW data. The simulation was made under the following conditions: sea water albedo; a standard midlatitude summer profile (*McClatchey et al.*, 1972); and the presence of aerosols with various values of ASSA (0 to 1), AAF (0 to 1), and AOD (0 to 0.5) at intervals of 0.01. The maximum AOD is set to 0.5 because about 98% of AOD is observed below this value over the ocean. Nevertheless, given the simulated RT efficiencies, ASSA and AAF values were estimated for all grid points with $\text{AOD} > 0.5$. Finally, we built a look-up table that relates the simulated RF efficiencies at the surface and the TOA to ASSA and AAF. The observed DRE efficiencies are compared with the simulated DRE efficiencies by a radiative transfer model to find the corresponding ASSA and g at 640 nm.

Figure 3.2a (for a constant $\text{AAF} = 0.65$ and various values of ASSA at TOA) shows that aerosol DRE decreases with an increase in ASSA for a given AOD. While the DRE is positive for $\text{ASSA} < 0.6$, this positive forcing may not occur in nature, because the extent of ASSA is known to be 0.90–0.99 (*Chin et al.*, 2002;

Andrews et al., 2006). For cases where $ASSA > 0.6$, the TOA DRE is negative and its corresponding DRE efficiency ranges from -60.9 to $-45.8 \text{ W m}^{-2} \text{ AOD}^{-1}$ (the slope for the shaded area). For a constant $ASSA = 0.95$ and various values of AAF, the TOA DRE increases with AAF (Fig. 3.2b). The sensitivity of DRE to AAF is greater than it is to ASSA, indicating that the scattering direction is more important than the scattering quantity at the TOA. It is to be noted that $AAF = 0.0$ means Rayleigh scattering, in which the strongest negative forcing is simulated. On the other hand, aerosols that are completely forward scattering ($AAF = 1.0$) have negligible forcing, because solar light penetrates the aerosol layer in the same direction. However, the extent of AAF is known to be 0.45–0.80 (*Chin et al.*, 2002; *Andrews et al.*, 2006), and the corresponding TOA DRE efficiency is between -99.0 and $-20.6 \text{ W m}^{-2} \text{ AOD}^{-1}$ (the slope for the shaded area).

At the surface, for a constant $AAF = 0.65$ and various values of ASSA, the DRE increases with ASSA (Fig. 3.2c). This is the opposite direction of the TOA DRE distribution. It is theorized that completely absorbing aerosols ($ASSA = 0.0$) result in a significant surface cooling of -250 W m^{-2} . For a constant $ASSA = 0.95$ and various g , we found that the surface DRE also increases with AAF (Fig. 3.2d). The Surface DRE is less sensitive to AAF than it is to ASSA, indicating that the scattering quantity is more important than the scattering direction at the surface. The DRE efficiency at the surface has a lower range than it does at the

TOA (-132.4 to $-79.5 \text{ W m}^{-2} \text{ AOD}^{-1}$ for $\text{AAF} = 0.65$, and -155.7 to $-67.9 \text{ W m}^{-2} \text{ AOD}^{-1}$ for $\text{ASSA} = 0.95$).

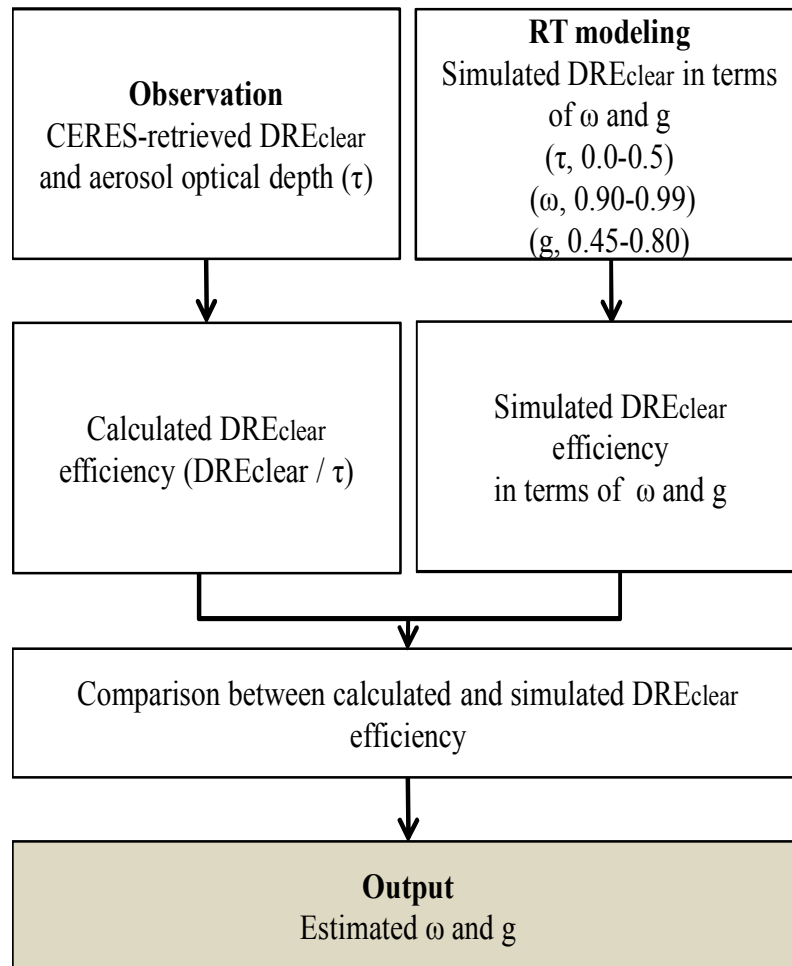


Figure 3.1. Flowchart to estimate the single scattering albedo (ASSA) and asymmetry factor (AAF) based on the CERES observation and radiative transfer model.

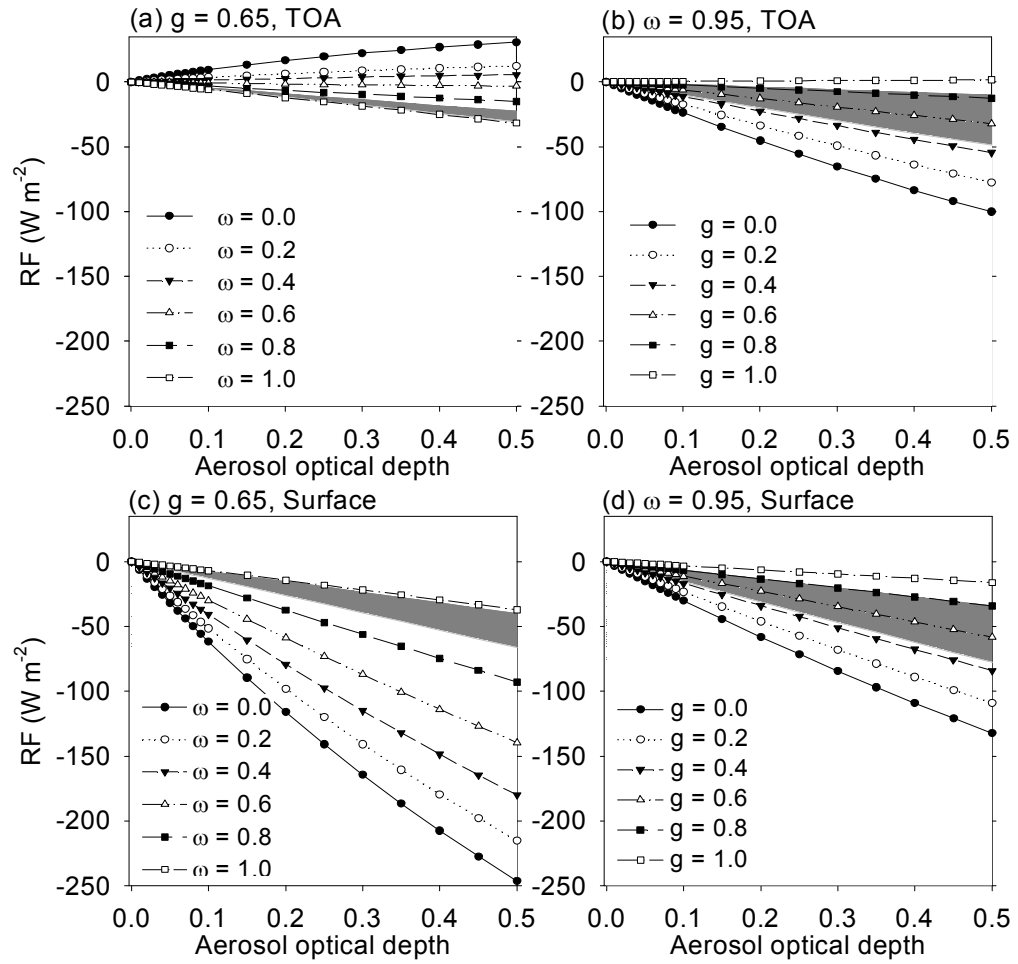


Figure 3.2. Simulated aerosol direct radiative effect in terms of aerosol optical depth for various ω and g at the TOA (a and b) and the surface (c and d). The shaded area denotes the existent range in observations.

3.3. Estimating aerosol direct radiative effect for all-sky

3.3.1. Direct radiative effect of total aerosol for all-sky

The method to calculate ΔDRE consists of three parts: (1) the look-up table composition from RTM simulations, (2) the input data preparation of satellite observations, and (3) the fitting of the input data into the look-up table (Fig. 3.3). The look-up table search is actually to relate the observed cloud properties with ΔDRE . In composing the look-up table, we used the Santa Barbara DISORT Atmospheric Radiative Transfer (SBDART) model (*Ricciazzi et al.*, 1998). The integrated spectral range was set to 0.3–5.0 μm , and the central wavelength to 0.63 μm , which is equivalent to those of the CERES spectrometer. The prescribed shortwave insolation in the SBDART model was scaled to the monthly observations of solar insolation in the FSW data.

Composition of the look-up table requires characterization of various cloud and aerosol properties: clouds with COD (0–20), ER (0–30 μm), and surface temperature (ST) minus CTT (0–60 K) at step size of 1, 1, and 5, respectively; and aerosols with AOD (= 0.2), aerosol single scattering albedo (ASSA = 0.87 or 0.99), aerosol asymmetry factor (AAF = 0.52 or 0.76). The simulated clouds are single-layered overcast clouds with spherical droplets since most of aerosols are not radiatively interacting with high-level cold clouds. The low (i.e., 0.87 and 0.55) and high (i.e., 0.99 and 0.76) values for ASSA and AAF represent various aerosol extents (*Chen et al.*, 2002; *Andrews et al.*, 2006), and an AOD of 0.2 used in the simulation is comparable to the global mean value (*Yu et al.*, 2006).

Later, ΔDRE s for the other ASSA and AAF values are calculated by bilinear interpolation at step size of 0.01 (0.01) due to the liner correspondence of ASSA (AAF) and ΔDRE (see *Choi et al.*, 2009). And also, ΔDRE simulated for AOD = 0.2 is scaled by the ratio of $(1 - \exp(AOD))$ to $1 - \exp(0.2)$ where AOD is the observed grid-mean value, to account for regionally varying AOD of non- or weakly-absorbing aerosols (*Zhao et al.*, 2011). The aerosol vertical profile is used obtained from CALIOP, which is determined by the ratio of the maximum pixel number of total aerosols among all layers to the pixel number of total aerosols in each layer. Here, the unit of the aerosol profile does not matter since the overall profile is exponentially scaled by the given AOD. For the atmospheric vertical profile, we set the temperature, water vapor, and ozone profiles for mid-latitude summer supplied in the RT model. However, these values do not matter because ΔDRE is nearly insensitive to these atmospheric profiles.

Using ΔDRE s and the corresponding cloud and aerosol conditions in the look-up table, we can get a third-order polynomial function relating all the variables:

$$\Delta DRE_{\omega,g} = a_{\omega,g}x^3 + b_{\omega,g}x^2 + c_{\omega,g}x + d_{\omega,g} \quad (7)$$

where ω is the ASSA, g the AAF, and x a cloud property (i.e., COD, ER, or ST minus CTT) in each grid cell. The coefficients a , b , c , and d are given in

Table 1. Eq. (7) indicates that the calculation of ΔDRE requires a grid-mean value of ASSA, AAF, and the cloud properties (COD, ER, and ST minus CTT) from the CERES/MODIS. Among these variables, cloud properties are directly measured by the satellite instruments, but the monthly-mean bulk aerosol properties (ASSA and AAF) should be retrieved in this study. This can be done by using shortwave flux and AOD from CERES (*Choi et al.*, 2009). In detail, DRE^{clear} efficiency (defined as aerosol DRE^{clear} per AOD) at both TOA and the surface as a function of ASSA and AAF is used to retrieve a pair (ASSA, AAF). The assumptions and conditions for the ASSA and AAF retrieval follow *Choi et al.* (2009). Since the ASSA and AAF values were derived from CERES observations, they should be physically consistent with the DREs. In comparison with ASSA and AAF from the AERONET ground observation, the uncertainties in ASSA and AAF are ± 0.03 and ± 0.05 , respectively (*Choi et al.*, 2009). The effects of these uncertainties on our estimate of aerosol DRE will be discussed in section 5.2. Note that high albedo and high uncertainties in observed cloud and aerosol properties at higher latitudes ($> 60^\circ$) preclude the calculation of ASSA, AAF, and finally ΔDRE . Over the relatively bright surface in the range of approximately 0.2–0.4, it is difficult to retrieve AOD which is essential to obtain ASSA and AAF because reflectance is virtually insensitive to AOD (*Seidel et al.*, 2012). Hence the present method is limited to low and middle latitudes and dark surfaces due to the relatively large retrieved uncertainty in AOD and DRE^{clear} efficiency for high surface albedo.

The sensitivity of ΔDRE to various aerosol and cloud properties was tested for quantitative examination of the cloud effects on aerosol DRE^{all} . Figure 3.3 shows ΔDRE -COD relation for different effective radius (ER; 10 and 30 μm), the difference between surface temperature and cloud top temperature (ST minus CTT; 10 and 30 K) and surface albedo (0.1 and 0.3). Figure 3.3a is for $ASSA = 0.87$ and $AAF = 0.52$ (i.e., strong absorbing and weak forward scattering). ΔDRE for $COD = 0.0$ refers to a zero cloud effect (i.e., $DRE^{all} = DRE_{obs}^{clear}$ in Eq. (3)). With the exception of very thin clouds ($COD < 2$), ΔDRE increases with increasing COD (i.e., optically thicker clouds), and a positive value for ΔDRE indicates offsetting the cooling effect of aerosols (Liao and Seinfeld, 1998). The negative slope for $COD < 2$ may be associated with solar radiation that is reflected or transmitted by thin clouds, and is scattered secondarily by aerosols. Particularly, more upward shortwave fluxes can pass through thin clouds for brighter surfaces at lower solar zenith angles, which induces negative ΔDRE . Moreover, relatively smaller ER or smaller ST minus CTT induce a larger ΔDRE for the same COD. It should be noted that the ΔDRE is mostly positive for low surface albedo (0.1; black lines), while negative for high surface albedo (0.3; gray lines). This is because the shortwave radiation reflected from a bright surface acts to strengthen the secondary scattering by aerosols. Conversely, Figure 3.3b is for $ASSA = 0.99$ and $AAF = 0.76$ (i.e., weak absorbing and strong forward scattering). The figure also shows the positive correspondence between COD and ΔDRE for $COD > 2$. For larger COD (>10), the positive slope is

diminished because a COD of more than 10 refers to thick clouds that completely block incoming solar radiation. However, ΔDRE is nearly insensitive to changes in ER and ST minus CTT.

Table 3.1. Regression coefficients for estimating ΔDRE as a function of the cloud optical depth (COD), effective radius (ER), and surface temperature (ST) minus cloud top temperature (CTT) for four pairs of (ASSA, AAF). Each value for (ASSA, AAF) at $0.63 \mu\text{m}$ is (0.87, 0.52), (0.99, 0.52), (0.87, 0.76), and (0.99, 0.76).

(ASSA, AAF)	x	a	b	c	d
(0.87, 0.52)	COD	-5×10^{-4}	-0.051	3.448	-30.62
	ER	-6×10^{-4}	0.047	-1.272	13.09
	ST minus CTT	-2×10^{-4}	0.037	-1.832	18.37
(0.99, 0.52)	COD	-1×10^{-3}	0.012	1.944	-37.85
	ER	-4×10^{-4}	0.034	-0.906	-8.680
	ST minus CTT	-5×10^{-6}	0.000	-0.022	-15.56
(0.87, 0.76)	COD	-5×10^{-4}	-0.026	2.227	-12.62
	ER	-4×10^{-4}	0.032	-0.897	17.42
	ST minus CTT	-3×10^{-4}	0.039	-1.910	26.28
(0.99, 0.76)	COD	-1×10^{-3}	0.046	0.449	-16.35
	ER	-2×10^{-4}	0.017	-0.472	-3.421
	ST minus CTT	-2×10^{-5}	0.002	-0.115	-6.117

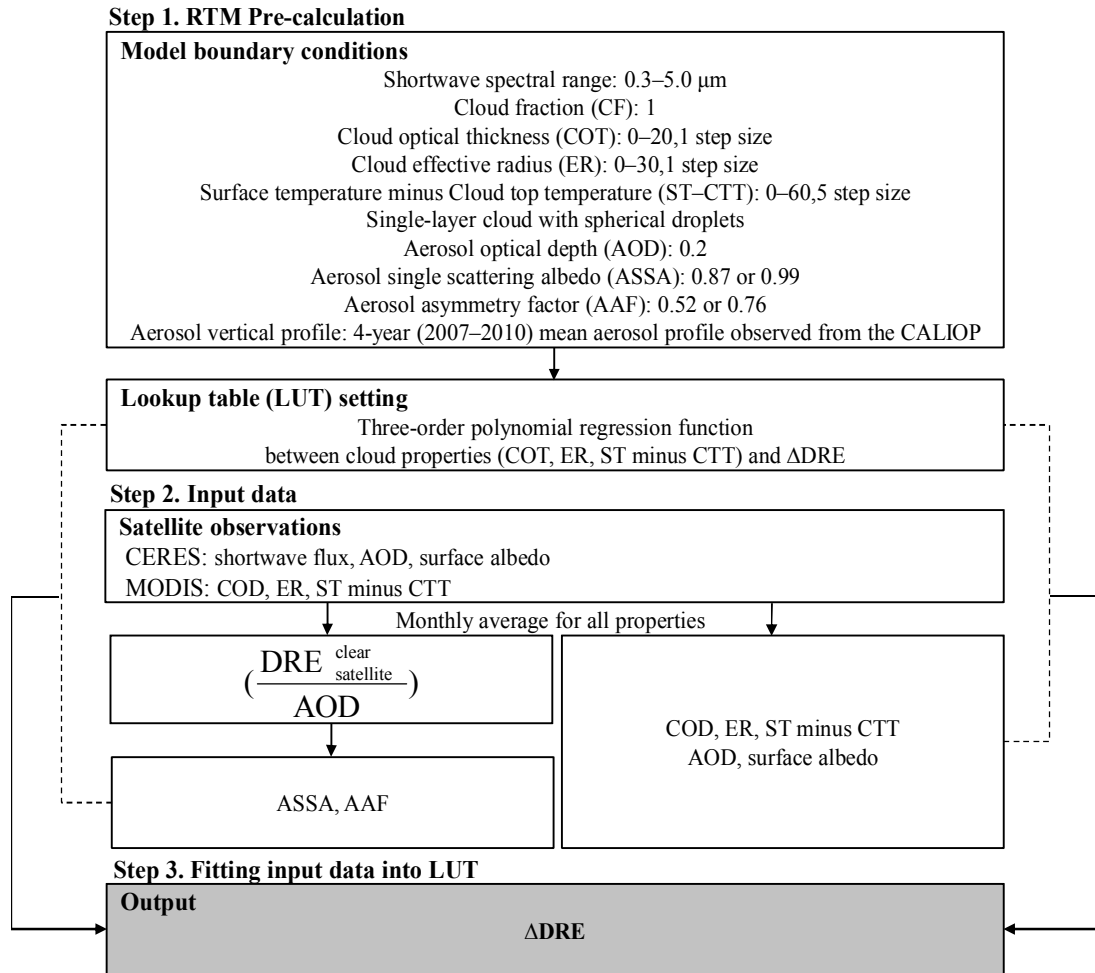


Figure 3.3. Flowchart for the methodology of estimating ΔDRE .

Simulated ΔDRE from RTM

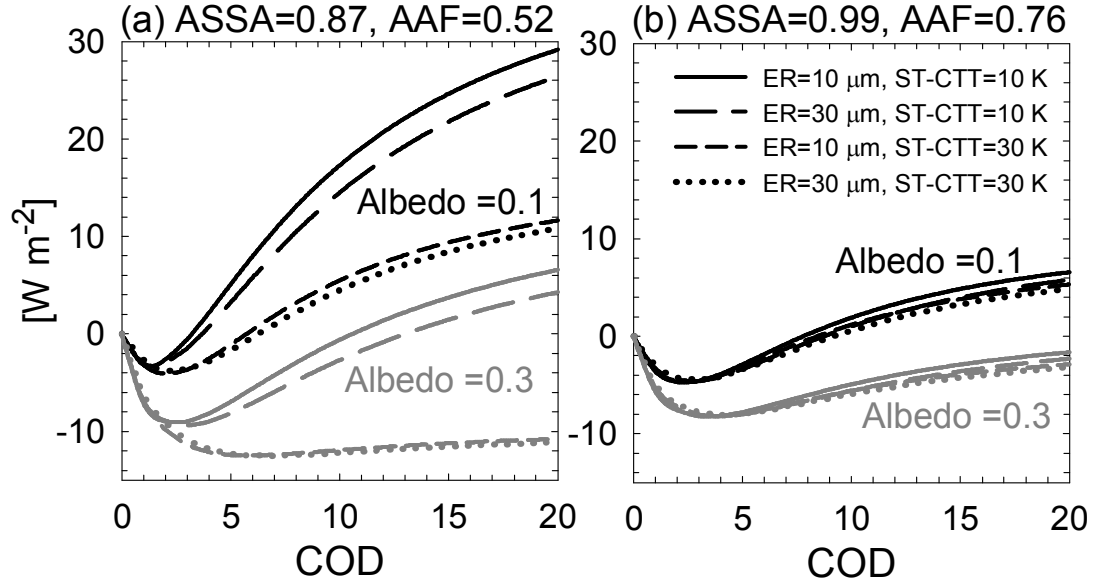


Figure 3.4. Simulated ΔDRE against COD for various ER, ST minus CTT and surface albedo for (a) ASSA = 0.87 and AAF = 0.52 and for (b) ASSA = 0.99 and AAF = 0.76. Black and grey lines denote surface albedos of 0.1 and 0.3, respectively.

3.3.2 Direct radiative effect of anthropogenic aerosol for all-sky

Aerosols can be divided into aerosols by anthropogenic and nature source. Between two type aerosols, anthropogenic aerosol mainly occurred in continent is role in an external source to perturb the earth's radiative balance (*Kaufman et al.*, 2005; *Bellouin et al.*, 2005). Therefore, there has been several tries to separate the effect by anthropogenic aerosol (ARF) from total aerosol radiative effect. For such reasons, we also examine the direct radiative effect by anthropogenic aerosol in all-sky condition based on the combined method as mentioned in section 3.3.1.

AOD of anthropogenic aerosol (AOD_{anth}) as an important input parameter to estimate ARF is determined by a method suggested in *Kaufman et al.* (2005). Namely, AOD of total aerosol is a sum of the anthropogenic, dust, and marine aerosol AOD.

$$AOD_{total} = AOD_{anth} + AOD_{dust} + AOD_{mar} \quad (9)$$

where AOD_{mar} is averaged AOD for marine aerosol for calm conditions, and its value is assumed to be 0.06 based on the AERONET and MODIS analysis. If AOD_{anth} is represented by anthropogenic (i.e., pollutant and smoke aerosol), dust, and marine aerosols, Eq. (9) is to be follows:

$$AOD_{total} = f_{anth}AOD_{anth} + f_{dust}AOD_{dust} + f_{mar}AOD_{mar} \quad (10)$$

where $f_{0.55}$, f_{dust} , f_{mar} , f_{anth} is FMF for total aerosol, dust aerosol, marine aerosol, and anthropogenic aerosol, respectively. Here, 6 unknown parameters are in the two equations and Eq. (10) can be arranged by Eq. (11).

$$\text{AOD}_{\text{dust}} = \frac{[(f_{0.55}\text{AOD}_{\text{total}} - f_{\text{anth}}\text{AOD}_{\text{anth}}) - f_{\text{mar}}\text{AOD}_{\text{mar}}]}{f_{\text{dust}}} \quad (12)$$

Under an assumption that the fraction of AOD by fine aerosol is constant for a give aerosol type, the values $f_{0.55}$, f_{dust} , f_{mar} , f_{anth} is 0.92, 0.51, and 0.32, respectively given in *Kaufman et al.* (2005). AOD_{anth} can be expressed as Eq. (13).

$$\text{AOD}_{\text{anth}} = \frac{[(f_{0.55} - f_{\text{dust}}) \times \text{AOD}_{0.55} - (f_{\text{mar}} - f_{\text{dust}}) \times \text{AOD}_{\text{mar}}]}{(f_{\text{anth}} - f_{\text{dust}})} \quad (13)$$

4. OCCURRENCE AND TRANSPORT MECHANISM FOR LASTING-DAY OF HIGH PM₁₀ EPISODES IN SEOUL

4.1. High-PM₁₀ days during 2001–2013:

4.1.1 1-day episode vs. multi-day episode

Based on the criteria for PM₁₀ concentration specified in environmental protection law in the Republic of Korea, high- PM₁₀ episodes are defined in this study using the daily-mean PM₁₀ threshold value of 100 $\mu\text{g m}^{-3}$. To distinguish the high-PM₁₀ episodes caused by the anthropogenic emissions from those caused by the natural phenomena such as Asian dust storms, yellow dust days (i.e., 114 days for 2001–2013), based on the announcement by the Korea Meteorological Administration (<http://web.kma.go.kr/eng/weather/asiandust/intro.jsp>), are excluded in this analysis. A total of 319 days of high-PM₁₀ episodes in the 13-year period that meet these criteria are selected for further analysis. Among 319 high-PM₁₀ days, 245 days (76%) were episodes that lasted for two to seven consecutive days, and 105 days (33%) were episodes that lasted for four or more consecutive days (i.e., multi-day). The daily average PM₁₀ concentration in these multi-day episodes exceeded 134.8 $\mu\text{g m}^{-3}$, which is nearly seven times the level (i.e., 20 $\mu\text{g m}^{-3}$) specified by WHO.

The differences in key specifics (such as emission sources and atmospheric transport) between multi-day and 1-day high-PM₁₀ days are examined below. Figure 1 shows that annual-mean PM₁₀ concentrations (○) decreased noticeably

over the analysis period, from $77.5 \mu\text{g m}^{-3}$ in 2002 to $41.1 \mu\text{g m}^{-3}$ in 2012, with high- PM_{10} days included in the multi-day (filled bars) and 1-day (open bar) episodes between 2001 and 2013. The total number of high- PM_{10} days (combined 1-day and multi-day episodes; total bar lengths in Fig. 4.1) also decreased during the period; indicating overall improvements in air quality in Seoul over this period. Despite the decline in the mean concentration and number of high- PM_{10} days however, the annual-mean number of deaths and inpatient admissions in relation to respiratory problems remained at the same level during the 13 year period. In addition, the number of high- PM_{10} days included in multi-day episodes remained similar between 2004 and 2013. Except for 2001 and 2003, multi-day high- PM_{10} episodes occurred about once or twice per year regardless of the annual-mean PM_{10} level, which amounts to approximately four to ten days in total. This implies that external factors (in addition to local emissions from the Seoul metropolitan area) are related to the occurrence of such multi-day high- PM_{10} episodes. In the case of unusually 2001, the multi-day episode was frequent (13 days) in late October and November because of relatively high PM_{10} mean level not in Seoul (\odot) and but in China (Wang et al., 2012) and continuously occurred and long lasting fog and haze.

Figure 4.2 shows the number of multi-day (filled bar) and 1-day (open bar) high- PM_{10} episodes with respect to season. There is a significant difference in the seasonal frequency of the both high- PM_{10} episodes. Compared to the frequency of 1-day episode, that of multi-day episode considerably differs to

each season. Particularly, the multi-day episodes most frequently occurred in the December–January–February period (DJF, 57 days of a total 105 days). The prevailing northwesterly wind in winter is found to be favorable for long-range transportation of air pollutants emitted from China to Korea (*Lee et al.*, 2011). Thus, analysis of atmospheric circulation characteristics, particularly pressure and wind distributions that affect the transport, dispersion, and accumulation of PM₁₀ during the high-PM₁₀ episodes are essential to gain an understanding of the occurrence of these multi-day high-PM₁₀ episodes, including the origins of the pollutants.

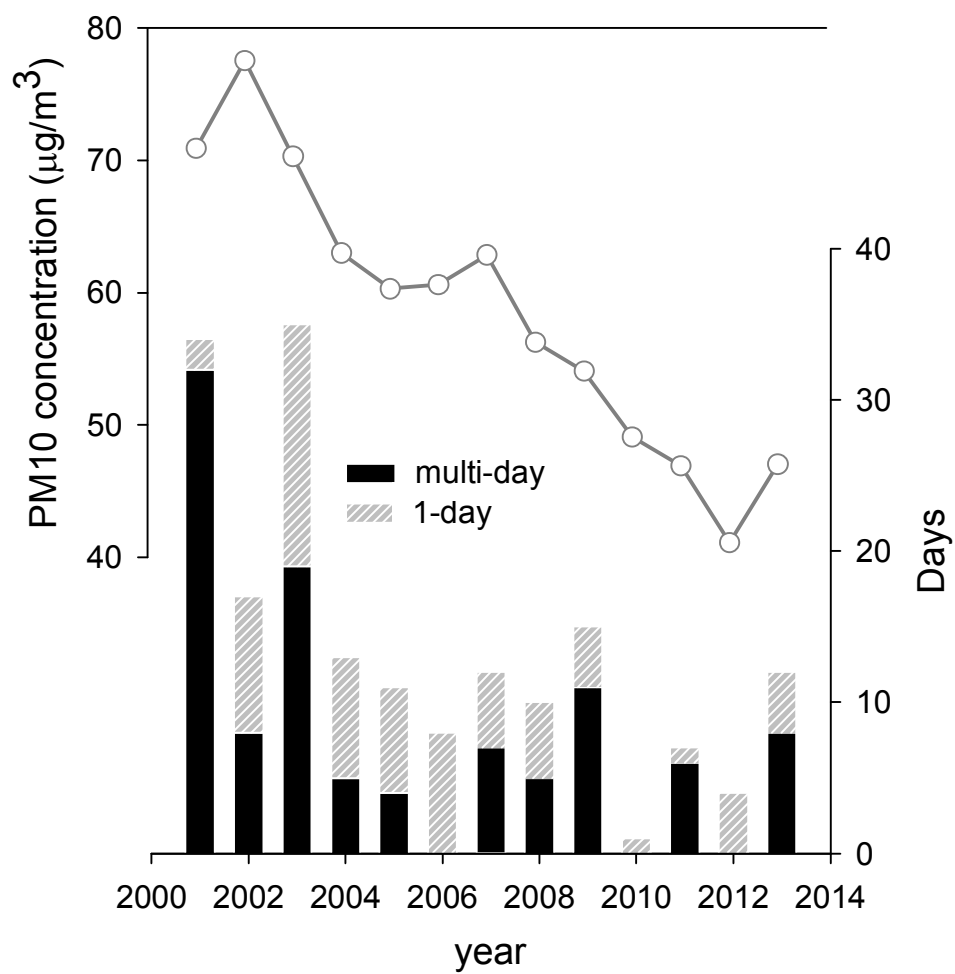


Figure 4.1. Annually averaged PM₁₀ concentration (○), days of high-PM₁₀ concentration episodes ($\geq 100 \mu\text{g m}^{-3} \text{ day}^{-1}$) from 27 air quality monitoring stations in Seoul. Black and grey bars denote the multi-day (≥ 4 days) and 1-day episodes in each year, respectively.

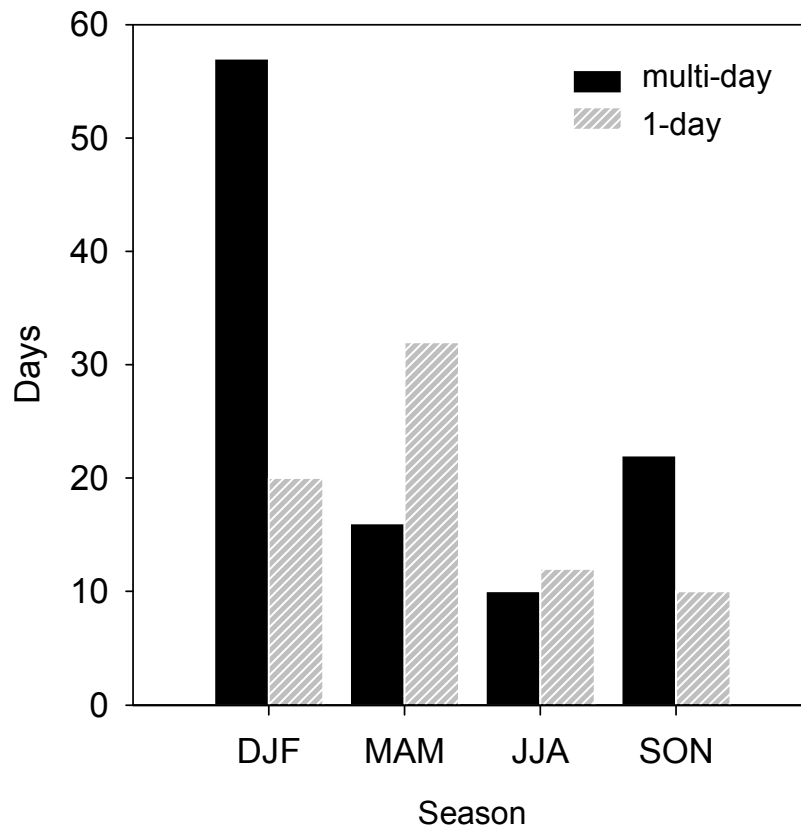


Figure 4.2. The number of high-PM₁₀ concentration days in each season. Black and grey bars denote multi-day and 1-day episodes, respectively.

4.2. Trans-boundary transport of PM_{10} from China to Seoul

4.2.1 Atmospheric circulation field

To identify the atmospheric conditions favorable for transporting air pollutants from the major source regions in China to Seoul during the multi-day high- PM_{10} episodes, we analyzed the large-scale atmospheric circulation on the pressure-longitudinal cross section along the latitude of 37.7°N that crosses Seoul on the onset dates of multi- or 1-day episodes (Fig. 4.3). To remove seasonality, monthly climatology has been removed from these atmospheric fields before analyses.

Figure 4.3 depicts the composites of anomalous geopotential height (a and e), vertical wind (b and f), zonal wind (c and g), and meridional wind (d and h) for the multi-day and 1-day episodes. Overall patterns are similar for these two types of episodes. As noted in previous studies, both types fulfill atmospheric conditions that are favorable for high- PM_{10} episodes in Seoul; e.g., high pressure anomalies and relatively weak winds near the surface. However, regional variations in magnitudes and features differ considerably from each other. For the multi-day episodes, relatively strong high pressure anomalies extend from the surface to the upper troposphere (Fig. 4.3a) across the eastern China–Korea region (also see Supplementary Figs. 4.3a and 4.3b). The high pressure system results in a general sinking motion (see the positive pressure velocity shown in Fig. 4.3b) which is favorable for high- PM_{10} concentrations near the surface, as air pollutants are trapped and transported from high levels to the surface. For the

1-day episodes, the relatively weak and narrow high pressure anomaly occurs above 700 hPa around 120° E, with a low pressure anomaly below 700 hPa over eastern China (Fig. 4.3e). Consequently, the anomalous low-pressure system leads to a vertically stretched rising motion to the west of 120°E (Fig. 4.3f). Therefore, massive amounts of air pollutants emitted from the major urbanized and industrial areas in eastern China can ascend by updraft and then descend by downdraft in the regions above the boundary layer over the region of Seoul. However, it is known that the transport of air pollutants within the boundary layer is weak.

We also identified a magnitude difference in the zonal wind field between the two episode types. Figure 4.3c shows a distinct decrease in the westerly above the 800 hPa level over China, Korea, and the neighboring western Pacific, implying anomalously stagnant conditions in the lower troposphere for the multi-day episodes. In contrast, Fig. 4.3g shows that an anomalously positive westerly occurs around Seoul between the surface and up to the 500 hPa level, indicating dispersion of air pollutants over a deep layer (about 5 km thick) in the lower troposphere. The general features of the meridional wind are similar for the two types of episodes: southerly and northerly over the left and right of 120° E, respectively (Figs. 4.3d and 4.3h). However, the southerlies over eastern China below 400 hPa for the multi-day episodes (Fig. 4.3h) are stronger than those for the 1-day episodes (Fig. 4.3a).

Figure 4.4 shows the horizontal distribution of anomalous geopotential height and wind field. The magnitude and intensity of anomalous high pressure system is clearly distinguishable between the two episodes. For the multi-day episode, both regions of the Korean Peninsula and China are highly affected by anomalous high pressure (Figs. 4.4a and 4.4b). Meanwhile, for the 1-day episode, the Korean Peninsula is seen to be affected by the rim of a high pressure anomaly with a center located near the East China Sea, whereas eastern China is located on a low pressure anomaly (Figs. 4.4c and 4.4d). Thus, the westerlies (southerlies) are more dominant for the multi-day (1-day) episodes (Figs. 4.4a and 4.4c, respectively), indicating that the atmospheric circulation during the multi-day episodes is more favorable for transporting pollutants from eastern China into Seoul than that occurring during 1-day episodes. In addition, for the multi-day episode, a strong anomalous low over northern Mongolia and western Pacific would play a major role in blocking the migratory anticyclone (Figs. 4.4a and 4.4b).

Through an analysis of the atmospheric fields above, we identified pressure and wind patterns that were more favorable for multi-day episode occurrences, and which could be considered as routes for moving air pollutants. In the multi-day episodes, PM_{10} is slowly transported in the lower troposphere from China to Seoul, while in the 1-day episodes ascending pollutants from eastern China are first transported via a relatively upper layer before descending over Seoul. The

following section presents further surface and satellite observation data in support of the evidence obtained through atmospheric field analysis.

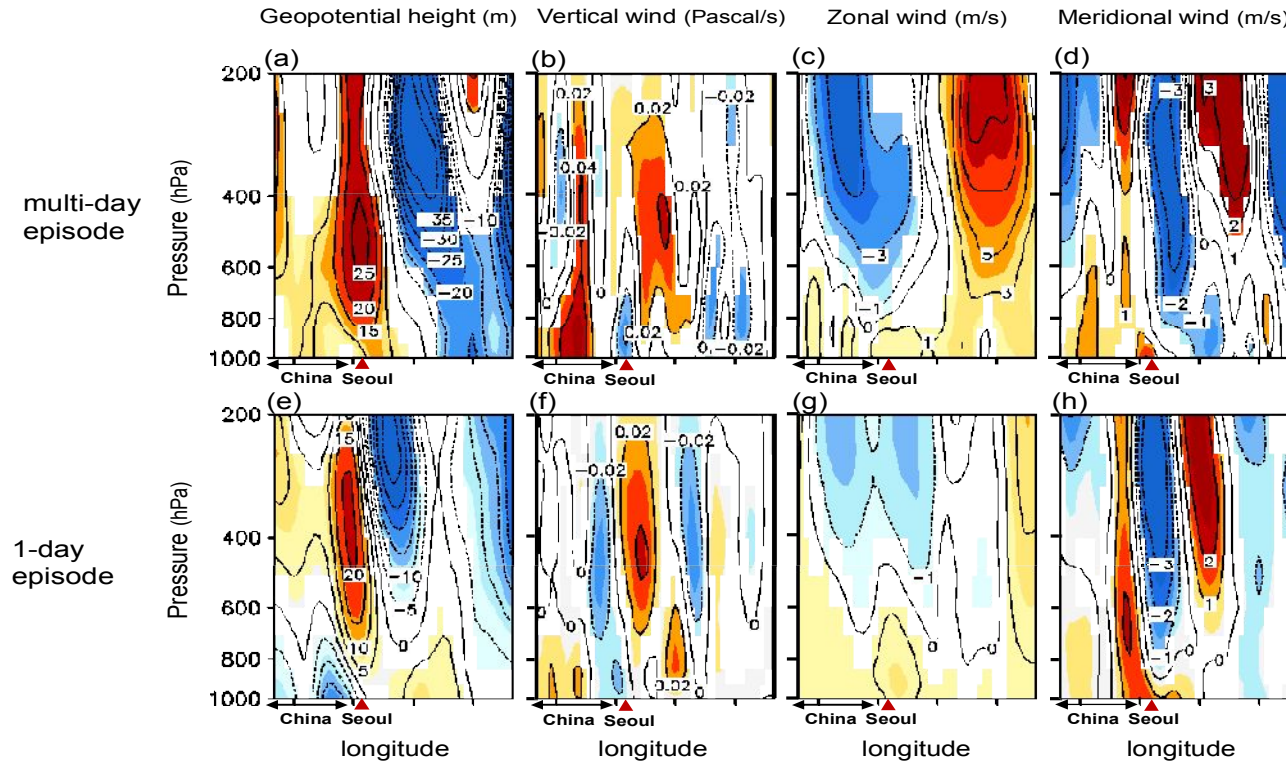


Figure 4.3. Composite of anomalous geopotential height (a and e), vertical wind (b and f), zonal wind (c and g), and meridional wind (d and h) at 37.5°N as functions of longitude and pressure on the onset day of multi-day (upper panel) and 1-day (lower panel) high-PM₁₀ concentration episodes.

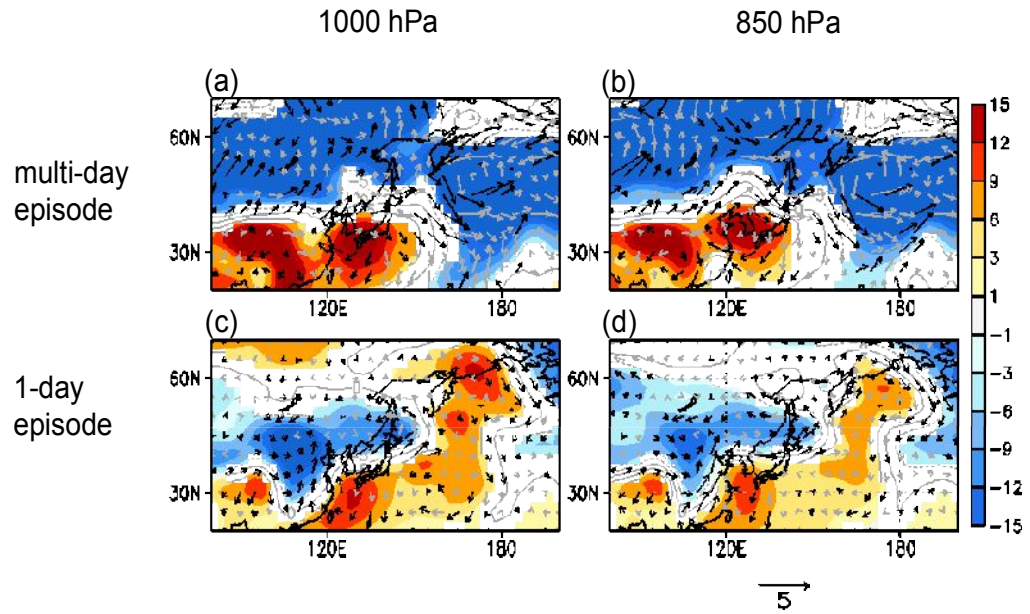


Figure 4.4. Composite of anomalous geopotential height and wind vector at 1000 hPa (a and c) and 850 hPa (b and d) on the onset day of multi-day (upper panel) and 1-day (lower panel) high-PM₁₀ concentration episodes. Shading denotes the regions significant at the 99% confidence level based on a t-test.

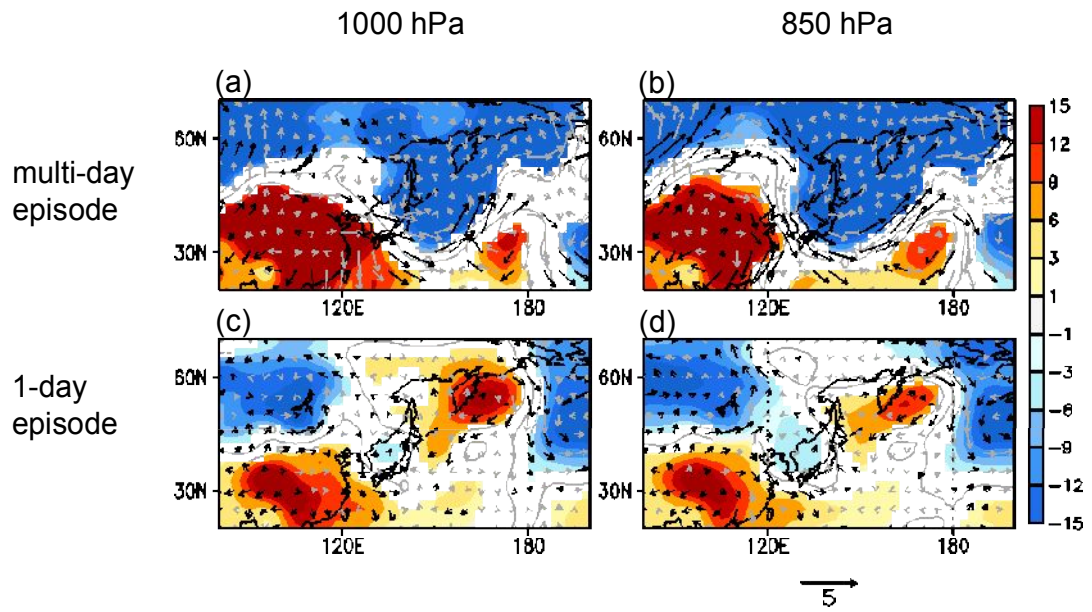


Figure 4.5. Same as Supplementary Fig. 4.4, except for -2 day high-PM₁₀ concentration episodes.

4.2.2 Station observations and backtrajectory analysis

To further clarify the results from the atmospheric field analysis for the two types of high-PM₁₀ episodes discussed in the previous section, we examined the air pollution index in China, the back trajectory (Fig. 4.6). It is notable that the relatively strong and large anomalous high across China and Seoul is favorable for the accumulation of air pollutants in the lower troposphere, and thus for high-PM₁₀ episodes.

We therefore analyzed the regional distribution of PM₁₀ concentration anomalies at 73 stations in China one day prior to both types of high-PM₁₀ episodes in Seoul (Figs. 4.6a and 4.6d). For both types of episodes, positive PM₁₀ anomalies are found at most of these stations, although in general there are larger positive anomalies for multi-day episodes than for 1-day episodes. Among the stations, the PM₁₀ levels in north- and middle-eastern China (e.g., Beijing, Tianjin, and Shanghai) are relatively high, indicating possible source regions of the multi-day high-PM₁₀ episode (Figs. 4.6a, 4.7a and 4.7b). The area-averaged PM₁₀ concentrations for multi-day and 1-day episodes are 207.3 $\mu\text{g m}^{-3}$ and 153.6 $\mu\text{g m}^{-3}$, respectively. In large areas of central and eastern China, the PM₁₀ concentration three days prior to a high-PM₁₀ multi-day onset in Seoul (Figs. 4.7a and 4.7b) was 80–160 $\mu\text{g m}^{-3}$ higher than the usual concentration one day prior to the onset (Fig. 4.6a). In particular, an anomalously high-PM₁₀ level over China occurring two and three days prior to episodes is evident during the cold season (October–March), perhaps due to the

increased use of heating fuel during anomalously cold periods. A maximum PM_{10} level occurring one day before the beginning of an episode in Seoul reflects the accumulation of pollutants by a high-pressure system. This therefore implies that for multi-day episodes, relatively large amounts of pollutants can be transported from China into the Seoul area.

In order to identify the aerosol pathways during the high- PM_{10} episodes in Seoul, we performed backward trajectory calculations using the NOAA HYSPLIT model at 500 m and 1000 m altitudes over a 72-hr period from the onset of each high- PM_{10} episode in Seoul. For this analysis, we divided each episode into cold (blue lines in the left panel figures) and warm seasons (April–September; red lines) in consideration of the seasonal difference in wind direction and speed. The number of high- PM_{10} days in cold and warm seasons is 75 (43) days and 30 (31) days for the multi-day (1-day) episodes, respectively. Figs. 4.6a and 4.6b (4.6d and 4.6e) show the mean horizontal and vertical pathways for the multi-day (1-day) episodes. The general feature shows that there is a longer pathway of air flow occurring at a relatively higher level in the cold season than in the warm season. This is common in both episode types, but the absolute path length of air varies according to the episode type. The trajectory is significantly shorter for the multi-day episodes than for the 1-day episodes, indicating relatively stagnant conditions, which is consistent with the very weak zonal wind field shown in Fig. 4.3c. Horizontal and vertical transport routes also vary for the different episode types. Among the severely polluted

regions (e.g., Beijing, Tianjin, and Shanghai) in China, the mean airflow passes through Beijing and Tianjin in China in multi-day episodes (Fig. 4.6a), but not in 1-day episodes (Fig. 4.6d). This means that air pollutants from Beijing and Tianjin may influence on occurrence of multi-day high-PM₁₀ episode in Seoul. In addition, on -2 day of the multi-day episode, northwesterlies are dominant in low troposphere along the east rim of the anticyclone located over China continent (Figs. 4.5a and 4.5b). As the anticyclone moves toward Korea on 0 day of the episode (Fig. 4.4), these pressure and wind may continuously contribute to the supply from China and the accumulation of air pollutants in Seoul. Furthermore, from -1 day of the multi-day episodes, the low tropospheric air flow paths are nearly horizontal from the Yellow Sea to the Seoul area, while they slant down from relatively higher levels in the 1-day episodes (Figs. 4.6b and 4.6e).

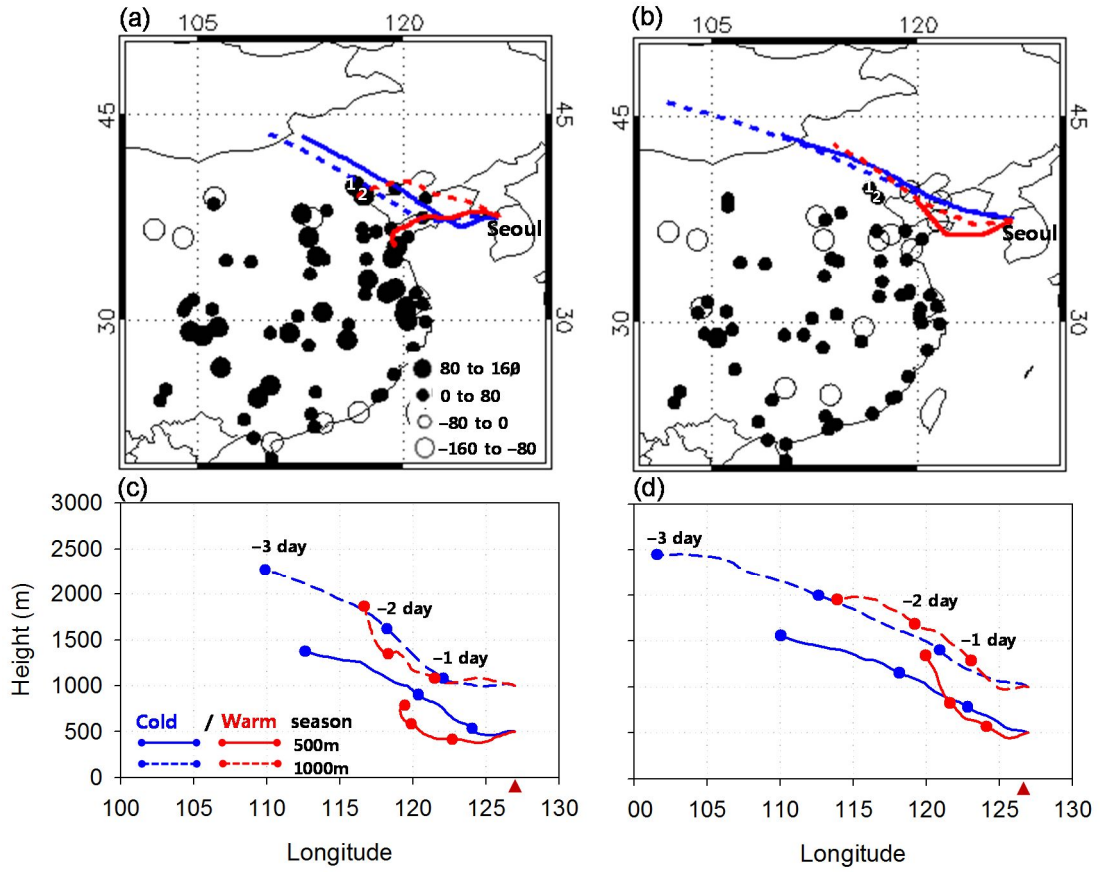


Figure 4.6. Spatial distribution (a and b) of anomalous PM_{10} concentrations measured from each of the 73 sites on -1 day of each high- PM_{10} episode, and 72-h wind back trajectory in cold (October–March; blue lines) and warm (April–September; red lines) seasons from the HYSPLIT model (a, c and d, d). The circle size in each figure denotes the anomalous PM_{10} concentration against monthly climatology, respectively. The stations in 1 and 2 in Figs. 4.6a and 4.6d are Beijing and Tianjin, respectively. Each closed circle is a 24 h interval in Figs. 4.6c and 4.6d.

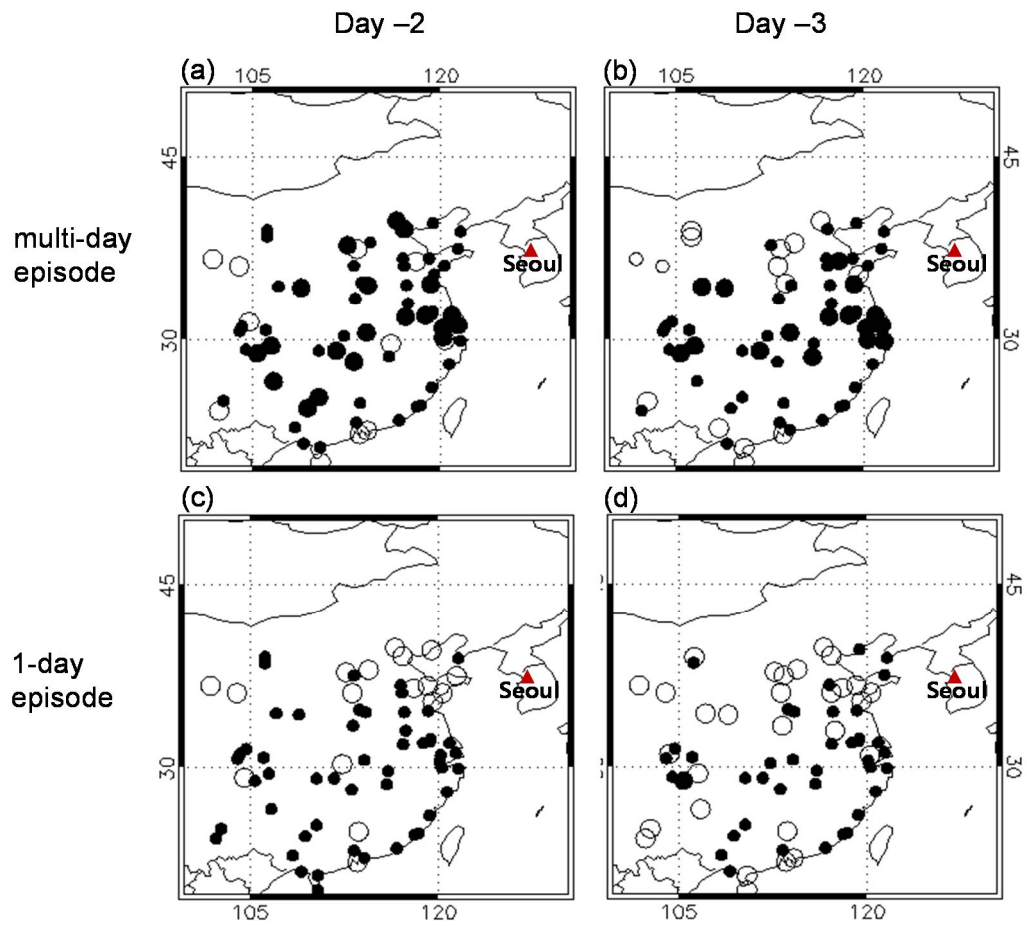


Figure 4.7. Spatial distribution of anomalous PM_{10} concentrations measured from each of the 73 sites on -2 day and -3 day of multi-day (a and b) and 1-day (c and d) high- PM_{10} episodes.

4.2.3 Satellite observed aerosol vertical profile

It was then considered that the difference in transport patterns may result in disparities in the aerosol vertical profiles between the two types of episodes in Seoul and its vicinity. We therefore further examined the aerosol profiles using the CALIOP vertical feature mask. However, because the data were only available after April 2006, we looked at seven and 31 onset days for the multi-day and the 1-day episodes, respectively. To extract aerosols over Seoul and its immediate neighboring areas, we only employed the CALIOP track data within ± 1.5 degrees from Seoul, both in latitude and longitude. Applying these criteria, three and ten collocated CALIOP tracks were identified for the multi-day and 1-day episodes, respectively, after April 2006. Although this analysis was limited by the small number of samples, it was considered beneficial to examine how aerosols were distributed in the vertical, as this was believed to provide independent and additional evidence related to the link between aerosol sources in East Asia, trans-boundary transport, and air quality in Seoul. Figures 4.8a and 4.8b show the aerosol pixel numbers for each level in each collocated case for the multi-day and 1-day episodes, respectively. There is a substantial difference in the vertical profiles between the two types of high-PM₁₀ episodes. Unlike in the 1-day episodes, where notable aerosol concentrations occur throughout the troposphere up to the 10 km level (Fig. 4.8a), in the multi-day episodes most aerosols are confined below the 1 km level (Fig. 4.8b), and this is closely related to the low-level accumulation of aerosols under stable atmospheric conditions

associated with a high-pressure system (Fig. 4.3a). This finding is also consistent with the back trajectory results (Figs. 4.6a and 4.6c); pollutants during the multi-day episodes are mostly spread within the boundary layer from the severely polluted regions of northeastern China. Aerosol profiles on the extended high-PM₁₀ episodes show high aerosol concentrations in the boundary layer. In conjunction with the low-level winds this suggests strong aerosol transport from northeastern China into the region. However, the situation is strongly contrasted for 1-day episodes, when the aerosol concentration in the low troposphere is much lower than for multi-day episodes: 1-day episodes are mainly caused by local emissions.

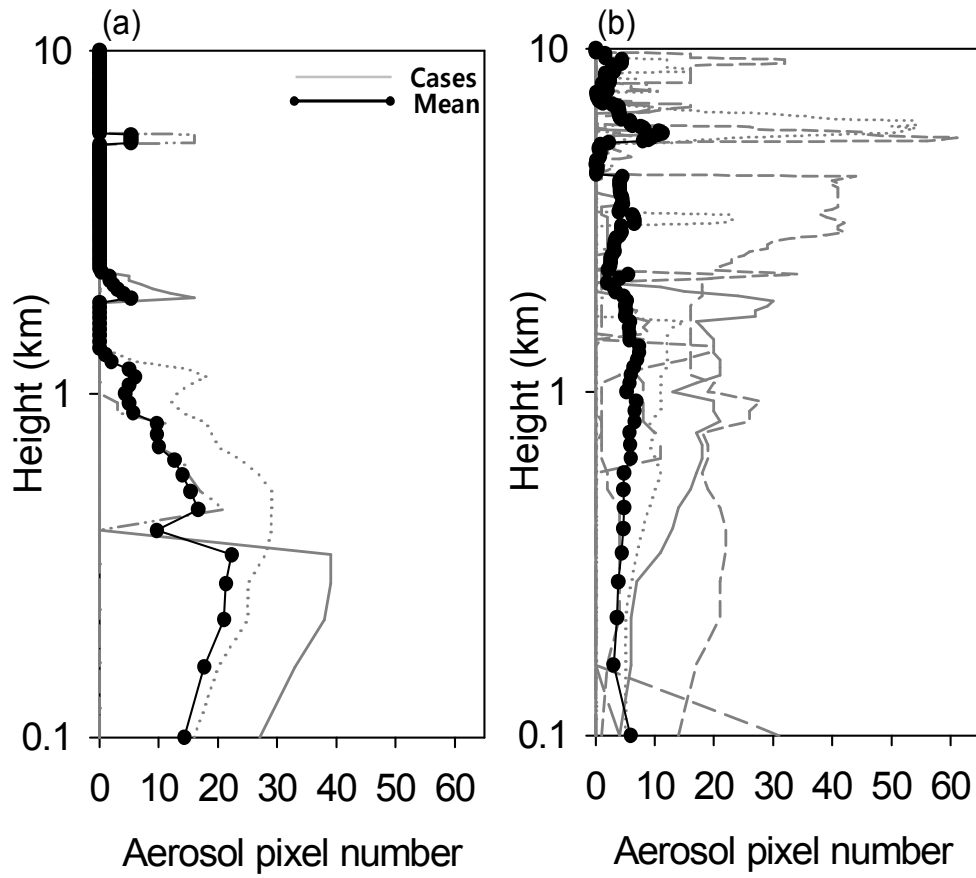


Figure 4.8. Vertical profile of aerosol pixel number for high-PM₁₀ concentration episodes from the CALIOP. Each line denotes a collocated case around Seoul for multi-day (a) and 1-day (b) episodes.

4.3. Summary and discussion

We examine the atmospheric circulations and resulting trans-boundary pollutant transports associated with multi-day (≥ 4 -day) high-PM₁₀ concentration episodes in Seoul, Korea. The meteorological conditions over East Asia on the onset dates of each episode type, the trajectories arriving at Seoul during episodes, and the horizontal and vertical distributions of aerosols over China and Korea before and after episodes strongly imply that the atmospheric circulation over eastern China and Korea, as well as the air pollutants emitted in northeast China, are closely related with multi-day high-PM₁₀ episodes in Seoul. Based on these analyses, we established a schematic diagram of multi-day high-PM₁₀ episodes (Fig. 4.9). This means that the atmospheric fields over China and its neighboring countries may determine the amount of air pollutants transported from eastern China into Seoul, and thus the duration of high-PM₁₀ episodes in Seoul. Compared to 1-day episodes, Seoul was found to be strongly affected by massive air pollutions over eastern China in the early stage of a multi-day high-PM₁₀ episode.

In this work, we focused on the beginning of high-PM₁₀ episodes in Seoul. However, it is considered that the process involved in the episodes and the end of multi-day episodes also need to be discussed. In this study, due to the lack of emission quantity data in Seoul, it was difficult to quantify the level of contribution from local emissions. Nevertheless, when it is taken into account that the episodes occur under the very strong anomalous high-pressure system and the

weak zonal wind in Seoul, it is suspected that local emissions may also cause further deterioration in the air quality within the city. It is examined that the large amount of PM₁₀ during an episode is eventually reduced either by precipitation > 0.5 mm (about 33 % of total episodes) via wet deposition, or in transport by the westerlies (in 1-day episodes, wet deposition by precipitation accounts for approximately 23 % of total cases).

It is noted that atmospheric circulations over the eastern China–Korea region and the PM₁₀ concentration in China (which are closely related to the duration of high-PM₁₀ episodes in Seoul) appear a couple of days before the onset of a multi-day episode (Figs. 6 and 7). Such circulations include strong and wide high pressure anomalies located in the lower troposphere over the entire region of China which enable: (1) favorable weather conditions for the occurrence of high-PM₁₀ levels in central and eastern China. As a result PM₁₀ concentration in eastern China increases from 3 days ago of the high-PM₁₀ episode and reaches its peak a day before its occurrence day; (2) strong anomalous low pressure conditions over the East Sea and the Okhotsk Sea to the east of the Korean Peninsula (which act as atmospheric blocking and further help conditions favorable for multi-day high-PM₁₀ episodes). Those indicate that the influence of China-originated air pollutants can be intensified under favorable atmospheric circulation condition. It is further considered that the presence of these precursors could be used to deliver advance warnings of multi-day high-PM₁₀

episodes, as well as enable air quality management in China to prevent future catastrophic air quality episodes in the interior and exterior of the country.

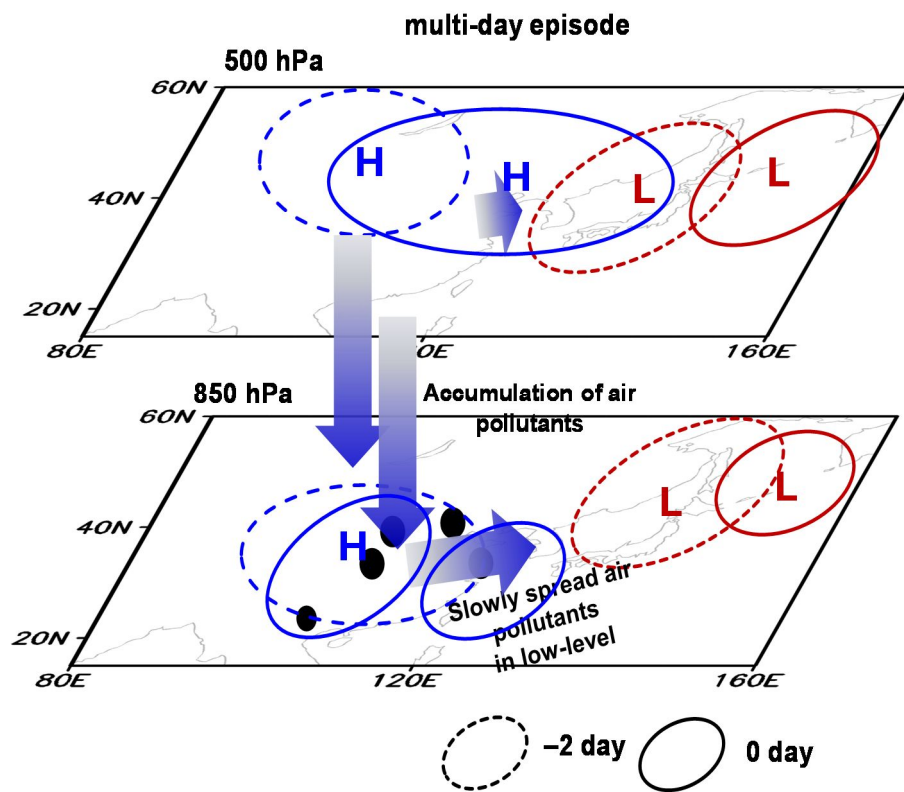


Figure 4.9. Schematic diagram of multi-day high-PM₁₀ episodes in Seoul, Korea.

5. ESTIMATED RADIATIVE IMPACT OF AEROSOLS FOR CLEAR- AND ALL-SKY

5.1. Influencing factors on aerosol radiative effect

5.1.1 Aerosol optical depth, aerosol single scattering albedo and aerosol asymmetry factor

Prior to estimate aerosol DRE^{all} , understand about various parameters as an input data has to be preceded, which is helpful to interpret role of each parameter on radiative process for all-sky. Therefore, we firstly analyze the various aerosol properties provided from several remote-sensing data.

Figure 5.1 shows the spatial distribution of columnar AOD and FMF retrieved from MODIS for the analysis period (2001–2005). The principal feature to note is that the larger values for AOD are distributed over the continental areas and its neighboring coastal areas. Particularly, high values (>0.5) of AOD for eastern China result from the combined effect by nature and anthropogenic aerosol (Fig. 5.1a and Fig. 1.2a). In addition, outflow areas of aerosol source regions are also substantially influenced by continental aerosols owing to easterlies or westerlies wind. By contrast, AOD is generally below 0.25 over the open sea. Alike the pattern of AOD, The overall pattern of FMF is similar to that for AOD (Fig. 5.1b). However, we note the relatively large FMF more than 0.6 over the southern China, Korea and Japan, which indicates most aerosols are constituted by small particles less than $1\ \mu m$.

As mentioned in section 3.3.2, we calculate AOD_{anth} over western North Pacific by using the MODS AOD and FMF, and the result is shown in Fig. 5.2. A spatial distribution of AOD_{anth} is similar to that for AOD and FMF. For the coastal regions of China, Korea, and Japan, the large industrial emissions result in the high values (≥ 0.15) of AOD_{anth} . This indicates a massive transport of fine-mode aerosols from the land into the open ocean. In comparison with previous studies, the magnitudes as well as the pattern of AOD_{anth} agree with those of *Bellouin et al.* (2005), *Yu et al.* (2009), and *Chen et al.* (2011). Considering that global averaged AOD_{anth} is 0.05, which is comparable with the value for *Chen et al.* (2011) with a bias of 0.01 over global ocean.

As mentioned in section 3.2.1, we estimated annual averages of ASSA and AAF over the globe, which are presented in Fig. 5.3. On average, relatively small ASSA (< 0.95) and AAF (< 0.66) are dominant over the continental and coastal sea, while the opposite is true over the open sea. This result means that more absorbing and backward scattering aerosols are present mostly over the land. This implies that more absorbing and forward scattering aerosol from the continent transport into the ocean. Consequently, transport of massive land aerosols derives an obvious gradient of aerosol properties in spite of equal oceanic area.

The present estimation is compared with the values obtained by *Kim and Ramanathan* (2008), who used the Georgia Tech/Goddard Global Ozone Chemistry Aerosol Radiation and Transport (GOCART) and assimilation with

the AERONET data. While the overall pattern of the two results is similar, the detailed regional magnitudes are found to be different. The magnitude of our ASSA and AAF estimates over the ocean were higher by 0.02–0.05 than the results from *Kim and Ramadathan* (2008), while that over the mid-latitude land is lower by 0.04–0.05. These discrepancies may have resulted from the difference of season, methodology, and measurement uncertainties between our study and their study. In this study, the estimated ASSA and AAF are the annual-mean, while the results from *Kim and Ramanathan* (2008) are the seasonal-mean of March to May that arise a number of the dust and smoke aerosols in the Northern Hemisphere. Methodologically their results are based on a chemical model, whereas our estimation was radiatively determined by the observed and RTM-simulated SW fluxes. The main advantage of our method is not only physical consistency with CERES data, but also that it is fast and demands little computing resources. However, it should be noted that the present method is limited to high latitudes and bright surfaces owing to the relatively large uncertainty of surface albedo.

In addition, the estimated ASSA and AAF are comparable with results from previous studies for the Pacific Ocean. For example, the ASSA around the East China Sea is 0.95, as obtained from the Asian Pacific Regional Aerosol Characterization Experiment (ACE-Asia) during the spring of 2001 (*Markowicz et al.*, 2003). The ASSA value is also 0.95 from observations over the remote Northern Pacific (*Takemura et al.*, 2002). The value of AAF is 0.69 over the

northern Pacific, from the simulation of *Kim and Ramanathan (2008)*. Note that these previous results are for the wavelength 550 nm, but our result is for 630 nm. However, the difference in the spectral dependence of light absorption by aerosols differs between 630 nm and 550 nm only on the order of the second decimal place (*Eck et al., 2001; Dubovik et al., 2002; McComiskey et al., 2008*)

To confirm the effectiveness of the estimated values, we validate the estimated ω and AAF values with the ground-based observations from AERONET sites. The results of the comparison are shown in Table 5.1. The estimates made by our method generally agree with the AERONET data within a bias of 0.03, with the exception of the g value from the Anmyon station. Slight upward or downward biases of ASSA are shown, and the downward biases of AAF are shown everywhere. The bias is due to a number of factors, such as different spatial resolutions, different viewing angles between the AERONET and satellite instruments, differences between the RT simulations, and other measurement uncertainties. We could not investigate the exact reason and source of this bias, however, because of a lack of observations in the western North Pacific. Nevertheless, none of the AERONET observations and the estimates of AASA and AAF over the coastal sea are greater than the estimated annual values over the open sea. Therefore, the distinction between the two regions remains clear and we examine the change in properties and radiative influence associated with aerosol transport in the next section.

The estimation is based purely on satellite-retrieved parameters and a near-real-time global value of aerosol optical properties is possible with this method. Moreover, the physical consistency in satellite-retrieved DRE and AOD data helps ensure that estimates on a grid basis are highly accurate. A global mapping of the distribution of aerosol optical properties by this method would be helpful in understanding not only the sources and transport mechanisms of the aerosol chemical compositions, but also the radiative impact of the aerosols on both regional climates and the global climate.

Table 5.1. Comparison of AERONET observations versus the estimations of single scattering albedo and asymmetry factor at Gosan (a), Osaka (b), Anmyon (c), and Taiwan (d). The standard error of the mean is also given.

Station		Sample number	Single scattering albedo (ω)		Asymmetry factor (g)	
			Observed value	Estimated value	Observed value	Estimated value
(a)	Gosan (126°E, 33°N)	6	-	-	0.68±0.01	0.65±0.01
(b)	Osaka (135°E, 34°N)	6	0.92±0.02	0.93±0.01	0.66±0.02	0.64±0.03
(c)	Anmyon (126°E, 36°N)	22	0.92±0.01	0.91±0.01	0.66±0.01	0.61±0.01
(d)	Taiwan (121°E, 25°N)	8	0.91±0.02	0.94±0.01	0.68±0.01	0.67±0.01

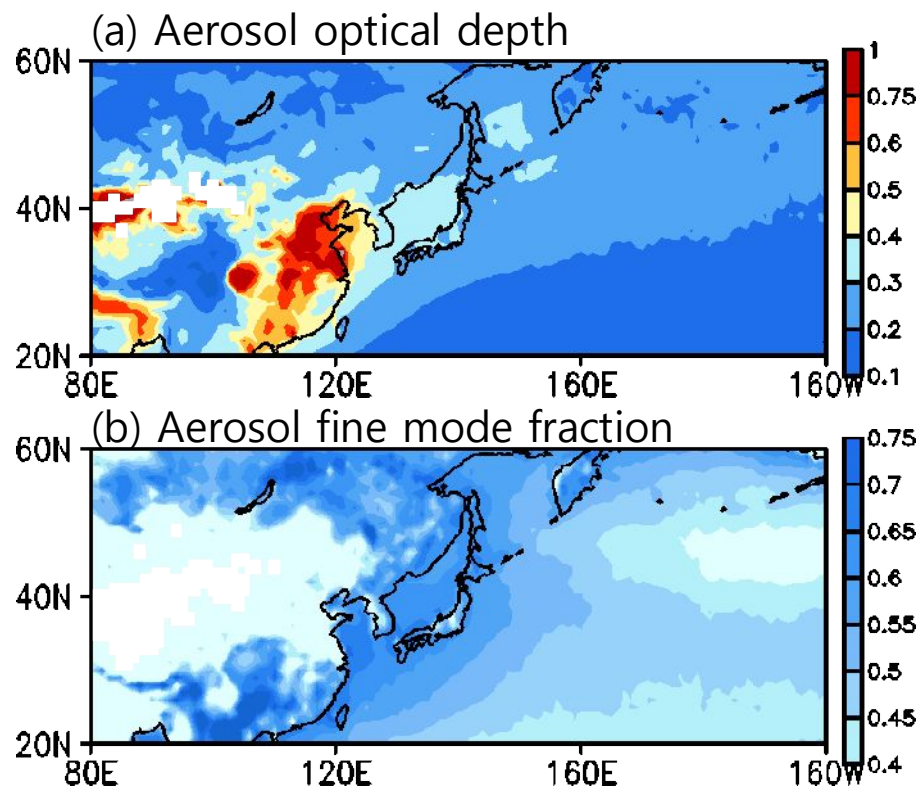


Figure 5.1. MODIS-observed annual-mean aerosol optical depth (a), and fine mode fraction (b) over East Asia (80°E–200°E, 20°N–60°N).

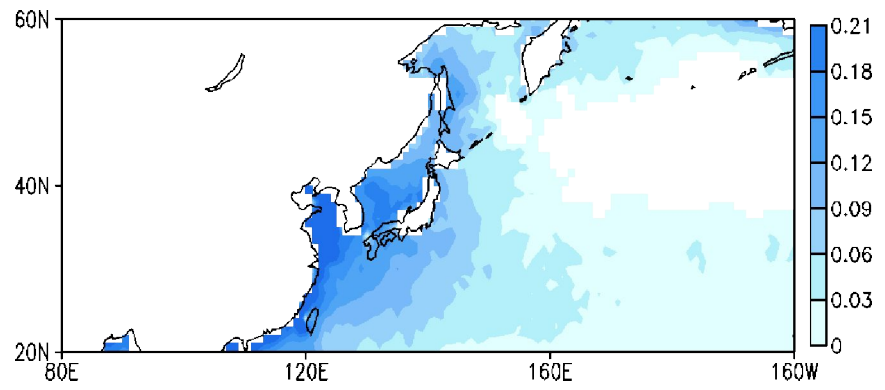


Figure 5.2. Spatial distribution of anthropogenic aerosol optical depth by the method suggested from Kaufman et al. (2005) over East Asia (80°E–200°E, 20°N–60°N).

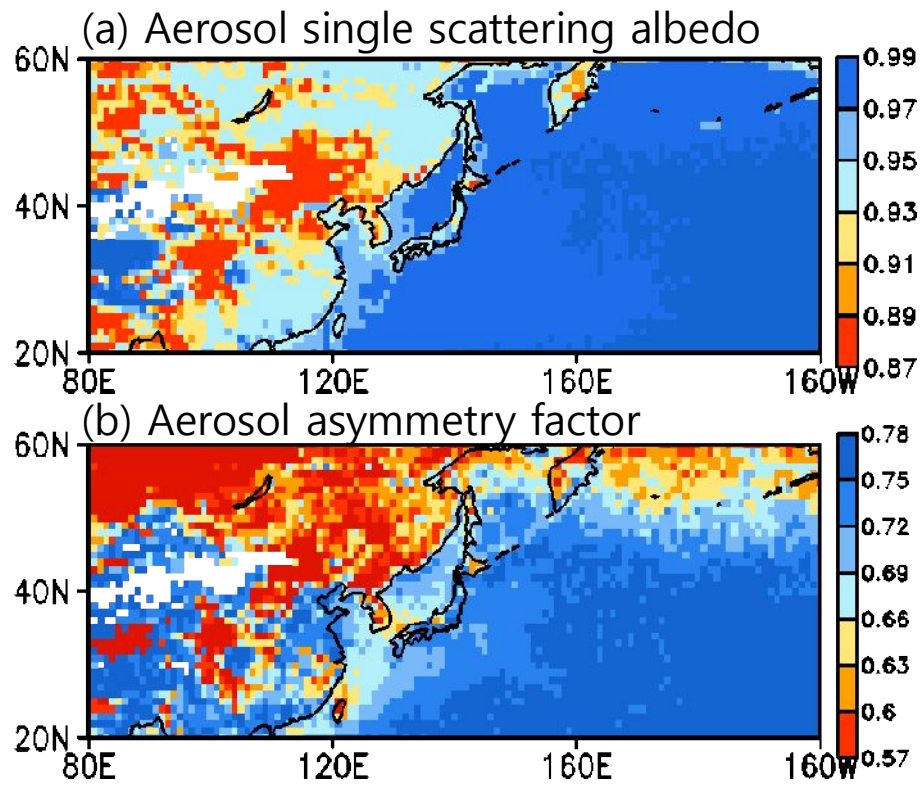


Figure 5.3. Spatial distributions of the estimated the annual average of (a) ASSA and (b) AAF over East Asia (80°E–200°E, 20°N–60°N).

5.1.2. Cloud fraction, cloud top temperature, cloud effective radius, and cloud optical depth

Cloud properties as another input data to calculate ΔDRE are obtained from the MODIS. Fig.5.4 shows the average of monthly averages for the entire period of (a) cloud fraction, (b) CTT, (c) ER and (d) COD. The domain (global) averaged value for the CF, CTT, ER, COD is 53.7 (51.0) %, 260.9 (264.8) K, 19.6 (19.6) μm , and 13.1 (11.4) respectively. The noteworthy feature in the figure is that the magnitude of all parameters is quite different between land and ocean. For the land, relatively low CF (< 0.6) is distributed while for the mid-latitude ocean high CF (≥ 0.7) is represented. The distribution of CTT is also similar to that of CF, implying that relatively high level cloud exists over the land compared to the ocean. CTTs are lower than 260 K over the western Pacific where deep convection frequently occurs. The magnitude of ER is also different between land and ocean. Small ER less than 15 μm is distributed over the land while relatively larger ER is spread over the ocean as the pattern of the CF. Meanwhile, pattern of COD differs with respect to the latitudes unlike other parameters. Relatively small COD below 10 prevails in the low latitude ($< 30^\circ$), on the contrary, large COD prevails in middle and high latitude ($> 30^\circ$). Note that the magnitude of COD over the East China where CF more than 0.6 is distributed is about twice (~ 15.5) as large as that over the equal latitude. The relatively larger COD and CF can imply that a possibility to reflect secondary effect of aerosol in this region (Lohmann and Feichter, 2005; Choi et al., 2008).

The spatial distribution of each parameter exhibits regional difference, implying the presence of quite different local influences of clouds on aerosol DRE^{all}.

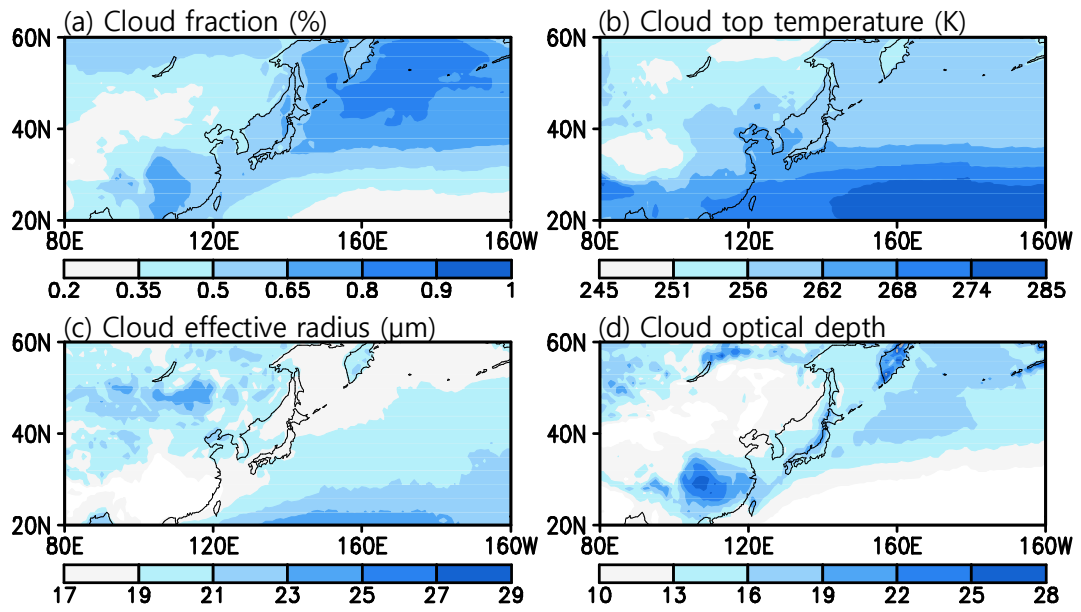


Figure 5.4. MODIS-observed annual-mean (a) cloud fraction (%), (b) CTT (K), (c) ER (μm) and (d) COD during year 2000–2005. The annual-mean is monthly averages of daily data for entire periods.

5.1.3 Aerosol vertical profile and its frequency above cloud from the CALIOP observation

It is well known that the aerosol vertical profile and the relative location between aerosol and cloud is significantly important to determine DRE^{all} . Therefore, first of all we examine the aerosol vertical profile of total and anthropogenic aerosol (i.e., polluted continental, polluted dust, and smoke) from the CALIOP during 2007–2010, and compared to the aerosol vertical profile from that suggested by McClatchey et al. (1972). Figure 5.5 shows the vertical distribution of anthropogenic (a) and total aerosol (b) for each year. The ratio in x-axis is the value for the pixel number of total aerosol in each layer divided by the maximum pixel number of total aerosol in a layer among the all layers. For inter-annual variability of each profile is very similar, and we expected that the influence of different time frame on our results is to be insignificant. For the profile of anthropogenic aerosol in Fig. 5.5a the vertical distribution shows two peaks in low level altitude less than 1 km (i.e., 0.4 km and 1 km), in which there is gradually decreasing aerosols above 1 km altitude. Similar with the profile of anthropogenic aerosol, total aerosol is dominant at low level under 1 km. Thus, we applied annual-averaged vertical distribution for four years (e.g., 2007–2010) from the CALIOP to estimate the all-sky DRE of aerosol.

Figure 5.6a shows various aerosol vertical profiles (lines) and the cloud layer at 2 km (blue shading). Profile 1 (black solid line) is the globally-averaged aerosol profile from CALIOP, characterized by two large values in the low

troposphere below 1 km (i.e., 0.1 km and 0.4 km); in this profile, most of aerosols are below the cloud. Separating a global ocean (dark gray line with open square) from global continent (gray line with open circle), we see their difference (gray shaded area). The aerosol maximum is at 0.1 km and 1 km over the ocean and the land, respectively. In addition, to understand sensitivity of ΔDRE to aerosol vertical profiles, we designated three other artificial aerosol profiles such that the aerosol ratios (defined as a ratio of the number of aerosol pixels at a level to the maximum over all levels) at 0.1–1.0 km in profile 1 are replaced at 2, 4, and 6 km, respectively. Hence, profile 2 (black dashed line) is of aerosols within the cloud, and profiles 3 (black dotted line) and 4 (black dashed–dotted line) are of aerosols above the cloud.

With the different aerosol profiles, the ΔDRE –COD relation was investigated for $ASSA = 0.96$ and $AAF = 0.70$ (Fig. 5.6b). Similar to the results in Fig. 3.4, a positive slope is shown in all of the cases for $COD > 2$. The slope is larger when aerosols exist at higher altitudes (profile 3 > profile 2 > profile 1). However, there is no difference between profiles 3 and 4, implying that ΔDRE is not subject to the altitude of aerosol located above the cloud. While not shown in the figure, the same is true for aerosol below the cloud. Simply put, the detailed aerosol profile is not so crucial in determining ΔDRE .

The relative altitude of aerosols to clouds are important to determine DRE^{all} , which is a factor to introduce an uncertainty in the aerosol DRE. We examined a frequency of aerosol occurrence above cloud over the globe from CALIOP VFM

data during 2007–2010. The frequency is determined by comparing maximum heights of aerosols and clouds from their vertical profile. Table 5.5 shows the percentage of six aerosol types and the frequency for aerosol above cloud, respectively. The total frequency with respect to each aerosol type is determined by the multiply between a comprised percentage to total aerosol and frequency of aerosol above cloud. The resulting total frequency by all aerosols is about 20% over the globe. The frequency of aerosol occurrence above cloud is relatively high ($> 20\%$) for clean continental, polluted dust, dust, and smoke aerosol. However, the occupied rate of clean continental aerosols to total is 9.31%, which is the smallest among six aerosol types.

In the radiative process between cloud-aerosol, the magnitude of the impact is largely dependent on the location of cloud and aerosol. (*Iorio et al.*, 2009). *Podgorny and Ramanathan* (2001) reported that the DRE at TOA is significantly sensitive both on the cloud properties and aerosol vertical distribution while that at surface is only sensitive on the cloud condition. For the aerosol mostly below clouds, cloud tends to decrease the reflection of solar radiation by aerosols back to space. Meanwhile for the aerosol mostly above clouds, cloud has stronger reflection due to increasing in albedo by the cloud. Atmospheric aerosols transport although the particle a relatively short residence time of 3–7 day on average, which induces the change in its properties and impact on the radiation. Therefore, we will show the radiative impact for a case of aerosol above cloud in the next section.

Table 5.2. Frequency (%) for aerosol above cloud from the CALIOP VFM data for four years (2007–2010).

Aerosol type	Percentage (%), A	Frequency for aerosol above cloud (%), B	Total frequency (%), A x B
Marine aerosol	27.22	9.56	2.60
Dust	21.85	35.77	7.81
Polluted continental	5.65	7.46	0.42
Clean continental	2.41	23.28	0.56
Polluted dust	30.91	24.35	7.52
Smoke	11.94	30.66	3.66
Total	99.99		22.59

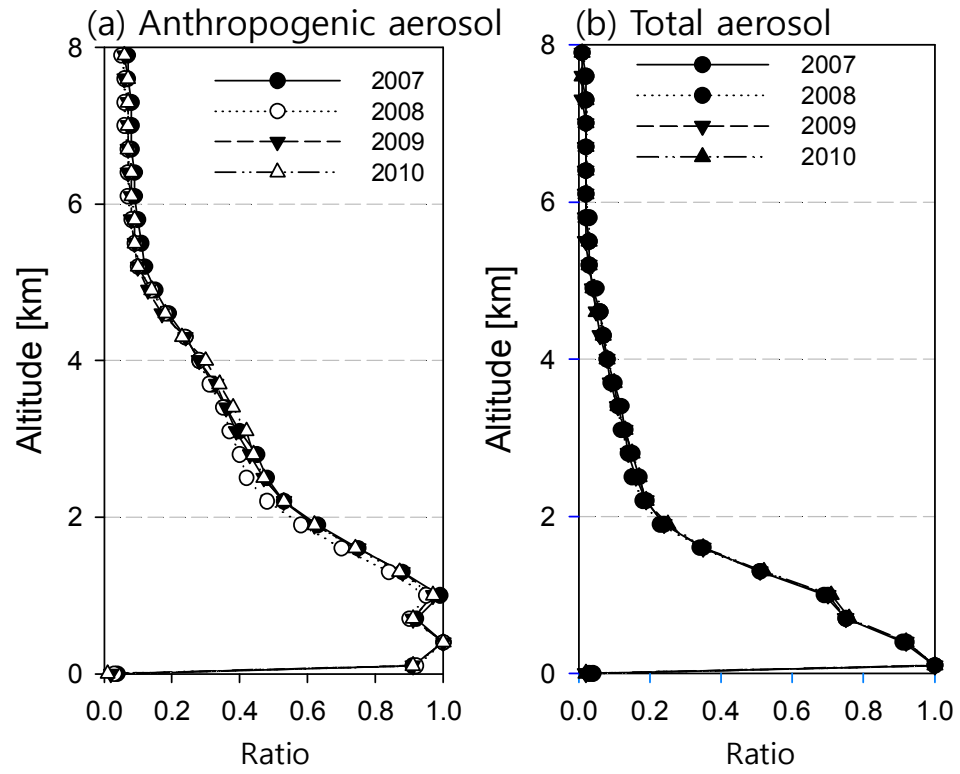


Figure 5.5. Annual-averaged vertical distribution of anthropogenic aerosols (a) and total aerosols for the period of 2007–2010 from the CALIOP.

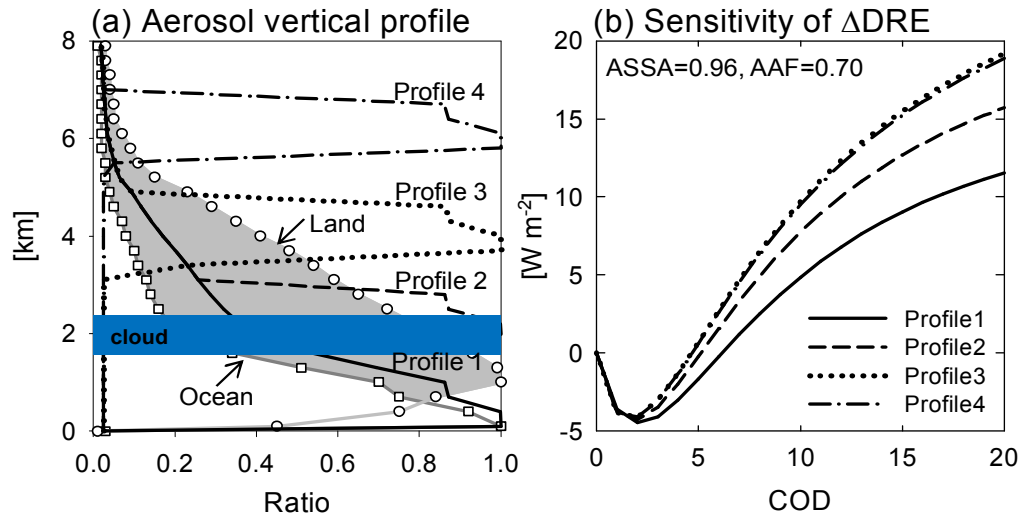


Figure 5.6. (a) Four aerosol vertical profiles and cloud layer at 2 km altitude (blue area) as the conditions of RTM experiments and (b) the simulated ΔDRE against COD for the different profiles. The ratio in x-axis indicates the value for the number of aerosol in each layer divided by the maximum number of aerosol in a layer among the all layers.

5.2. Direct radiative effect of total and anthropogenic aerosols

5.2.1 Direct radiative effect of total aerosol

In presence of clouds, the radiation processes are complicated because of scattering and absorption not only by aerosol but also cloud. Particularly cloud is one of the important factors to control earth's radiative balance as well as it induces uncertainty in examining DRE of aerosol. Therefore to assess the DRE of aerosol for all-sky, it is necessary to understand about the aerosol-cloud interaction on the radiative process. For the reason we explain the radiative relationship between aerosol and cloud in this section.

Figure 5.7 shows the spatial patterns of annual-averaged aerosol DRE^{clear} (a), ΔDRE (b) and DRE^{all} (c). In general, DRE^{clear} is found to be $< -5.0 \text{ W m}^{-2}$ in most regions, indicating a dimming effect due to aerosols (Fig. 5.7a). It is clear that DRE^{clear} is stronger over the eastern China, Korea, Japan, and neighboring coastal sea and weaker over the open sea. The DRE^{clear} pattern is similar to that of the MODIS AOD and FMF, implying that DRE^{clear} is characterized mainly by the masses and types of the aerosols. The area-averaged aerosol DRE^{clear} values \pm standard deviation were -9.3 ± 2.1 . The result is comparable to the previous studies. For example, over the global ocean, DRE^{clear} is $-5.7 \pm 1.7 \text{ W m}^{-2}$ from MODIS aerosol properties and CERES irradiance (*Christopher and Zhang, 2004; Zhang et al., 2005*) and it is -6.8 W m^{-2} according to the *Bellouin et al. (2005)*. *Zhao et al. (2011)* reported that aerosol DRE for clear-sky condition is to

be $-6.8 \pm 1.7 \text{ W m}^{-2}$ from the combined approach of CERES/MODIS and GOCART model, which was comparable with our results. The slight discrepancy between two results may have resulted from the estimating flux for pristine condition. We used a flux for pristine condition in each grid from the CERES/FSW, while *Zhao et al.* (2011) calculated it when AOD equal to zero with respect to solar zenith angle and near surface wind. Also, the magnitude for *Zhao et al.* (2011) is 24-h averaged value, but that for this study originates from instantaneous measurements at overpass time of Terra satellite.

The ΔDRE has generally positive sign over the ocean (Fig. 5.7b). For the white regions the ΔDRE could not be derived because ASSA and AAF were not estimated over bright surfaces. The area-averaged values of ΔDRE were 6.3 ± 2.5 . There is a distinct difference between land and ocean, which may be due to the different surface albedo. As aforementioned in Fig. 3.4, more shortwave radiation is reflected over bright than dark surfaces reinforcing scattering by aerosols and their cooling effect. On the contrary, for dark surfaces such as the ocean with a low surface albedo, clouds compensate for a negative aerosol $\text{DRE}^{\text{clear}}$. Especially over the ocean at latitudes higher than 30° N , ΔDREs are significantly large ($> 12 \text{ W m}^{-2}$), primarily due to the large COD (compare Fig. 5.7b with Fig. 5.4). It is recalled that the COD and CF are major factors to increase the ΔDRE . Positive values of ΔDRE can also be found over south east Asia, probably because these regions have low surface albedo due to abundant vegetation and crop compared with other land regions.

Fig. 5.7c shows the spatial pattern of the aerosol DRE^{all} . When comparing DRE^{all} with DRE^{clear} , aerosols still have a net cooling effect over land. In particular, DRE^{all} over eastern Asia is significantly strong cooling effect ($\leq -15 \text{ W m}^{-2}$). For ocean at lower than 30° N have relatively weak net cooling effect. However, for the extratropical oceans, the sign of the aerosol DRE turns out to be positive. The area-averaged DRE^{all} values \pm standard deviations were -3.5 ± 2.3 . Our result was in a good agreement with the global value (-3.0 W m^{-2}) from model-based estimation by *Kim and Ramanathan* (2008) and that (-2.9 W m^{-2}) for combining approach from the CERES/MODIS and GOCART by *Zhao et al.* (2011).

The monthly variations in the aerosol DRE^{clear} and DRE^{all} over nine regions including East Asia (Fig. 5.6) were also investigated. The nine selected regions as follow; Mediterranean basin (a), India (b), East Asia (c), West coast of U.S.A. (d), East coast of U.S.A. (e), West coast of North Africa (f), Australia (g), Amazon basin (h) and Southern hemisphere ocean (i). The monthly variations and magnitudes of both DRE^{clear} and DRE^{all} exhibited regional differences, reflecting the different aerosol sources and emission quantities, as well as the different cloud effects on aerosol DREs. Overall, DRE^{all} was smaller in magnitude than DRE^{clear} , with the exception of DJF for India and Australia. For India, East Asia, and West coast of North Africa, both DRE^{clear} and DRE^{all} show large seasonal variations. Furthermore, the difference between DRE^{clear} and DRE^{all} was relatively small during DJF, but relatively large during JJA.

Over West coast of U.S.A., East coast of U.S.A. and Amazon basin, the differences between DRE^{clear} and DRE^{all} appear relatively small, being nearly equal in Australia, and almost no seasonal pattern is observed. In particular, over Southern hemisphere ocean, the differences is much larger ($> 6.5 \text{ W m}^{-2}$) than that over other regions and the variations were considerably different due to storms in the Southern Hemisphere, implying that clouds can modify the DRE^{clear} in this region.

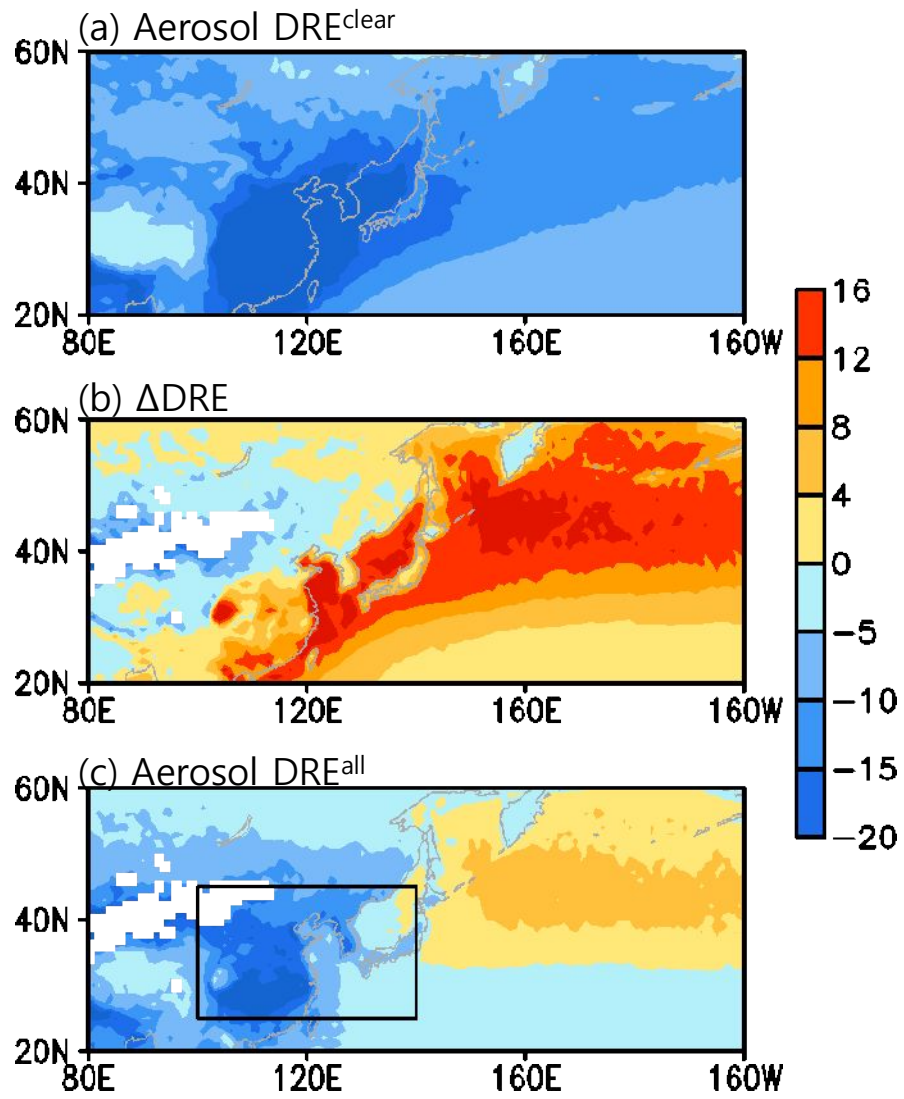


Figure 5.7. Spatial distributions of the annual-averaged (a) aerosol DRE^{clear}, (b) Δ DRE (c) aerosol DRE^{all}.

Aerosol DRE for clear-sky and all-sky

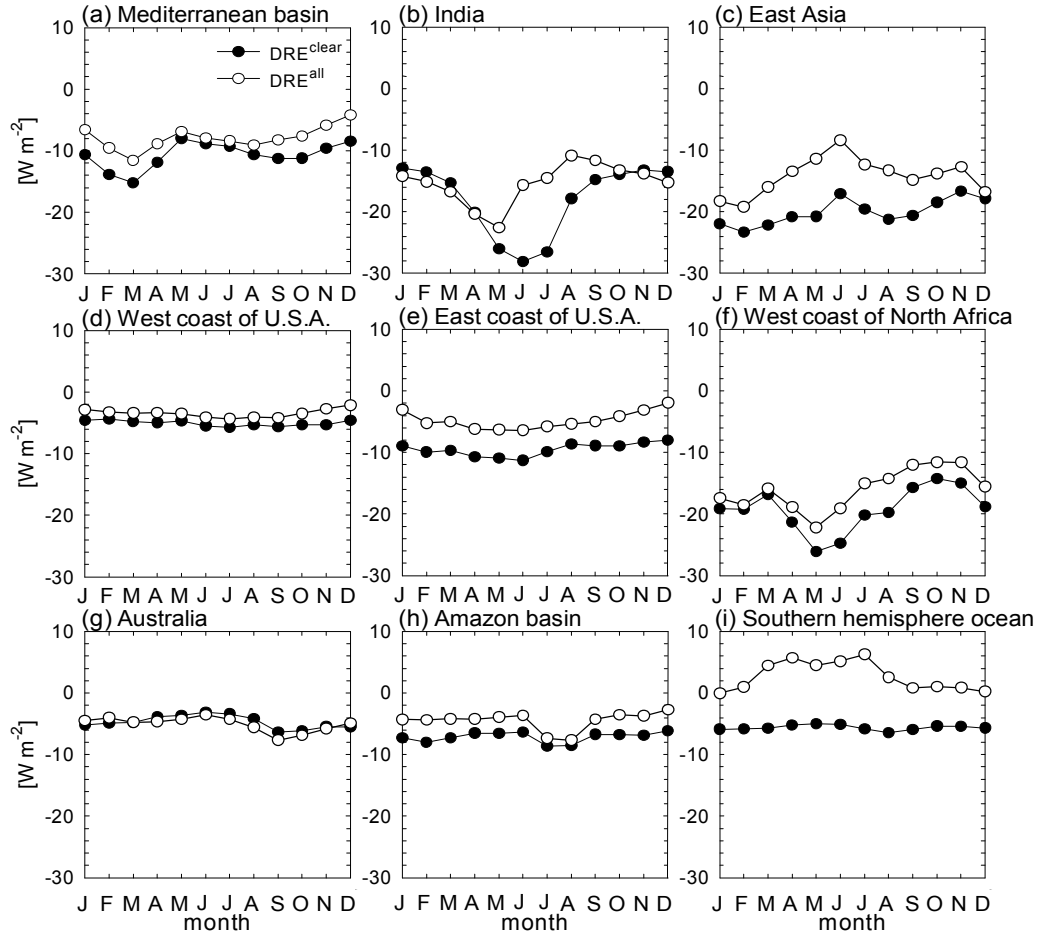


Figure 5.8. Monthly variations in the aerosol DRE^{clear} and aerosol DRE^{all} over the nine regions. The closed and open circles denote the aerosol DRE^{clear} and DRE^{all} , respectively. The nine regions are denoted as follow; Mediterranean basin (a), India (b), East Asia (c), West coast of U.S.A. (d), East coast of U.S.A. (e), West coast of North Africa (f), Australia (g), Amazon basin (h) and Southern hemisphere ocean (i).

5.2.2 Direct radiative effect of anthropogenic aerosol

The seasonal averages of ARF^{all} obtained from Eq. (1) (ARF_1^{all}) and Eq. (2) (ARF_2^{all}) and their differences are presented in Fig. 5.3. The seasonal distributions of ARF_1^{all} (Figs. 5.3a–5.3d) mostly coincided with results from *Chen et al.* (2011). Relatively large cooling effects ($\leq -3 \text{ W m}^{-2}$) occur in neighboring coastal sea of the Middle East, India, East Asia, Mexico, and Colombia. The annual average \pm standard deviation of ARF_1^{all} is $-0.42 \pm 0.40 \text{ W m}^{-2}$, which is slightly smaller than $-0.34 \pm 0.16 \text{ W m}^{-2}$ in *Chen et al.* (2011). The minor underestimation of ARF_1^{all} in this study may have resulted from two reasons as follows. Firstly, we used a flux for pristine condition in each grid from the CERES/FSW, while *Chen et al.* (2011) calculated it by linear extrapolation to zero of aerosol optical depth (AOD) with respect to solar zenith angle and latitude. Secondly, in this study, ARF_1^{all} is instantaneous value since all input data of aerosol and cloud to obtain ARF_2^{all} from Eq. (2) are instantaneously measured at overpass time of Terra satellite, though ARF_1^{all} for *Chen et al.* (2011) is the daily average. Consequently, the methodology in this study, though it is somewhat different from that of *Chen et al.* (2011), is on account of fair comparison between ARF_1^{all} and ARF_2^{all} .

When influence of cloud on ARF in cloudy regions is considered, the spatial patterns of ARF_2^{all} are shown in Figs. 5.3e–5.3h. The overall patterns of a dimming effect by anthropogenic aerosols and its seasonal variation are similar

with those in Figs. 5.3a–5.3d. However, the cooling effect by the aerosols is fairly diminished across the whole season, which is remarkable over the mid-latitude ocean. The annual mean \pm standard deviation of $\text{ARF}_2^{\text{all}}$ is $-0.06 \pm 0.82 \text{ W m}^{-2}$. The smaller $\text{ARF}_2^{\text{all}}$ compared to $\text{ARF}_1^{\text{all}}$ reflects that cloud, especially optically thick and a large amount cloud, could interrupt the radiation back to space by aerosols and could modify direct radiative effect by aerosols (*Chand et al.*, 2009).

Figures 5.3i–5.3l display the difference between $\text{ARF}_2^{\text{all}}$ and $\text{ARF}_1^{\text{all}}$, indicating cloud impact on ARF^{all} . It is noted that sign of $\text{ARF}_2^{\text{all}} - \text{ARF}_1^{\text{all}}$ is positive over whole ocean because of cloud influence which blocked out the scattering by anthropogenic aerosol. The annual mean \pm standard deviation of $\text{ARF}_2^{\text{all}} - \text{ARF}_1^{\text{all}}$ is $0.65 \pm 0.63 \text{ W m}^{-2}$. $\text{ARF}_2^{\text{all}} - \text{ARF}_1^{\text{all}}$ is small ($\leq 0.2 \text{ W m}^{-2}$) in low-latitude and large ($> 2 \text{ W m}^{-2}$) in mid-latitude particularly for summer in northern hemisphere, implying that cloud effect on $\text{ARF}_2^{\text{all}}$ is more significant over mid-latitude than over low-latitude.

Table 5.2 shows seasonally area-averaged values of AOD, AOD_{anth} , $\text{ARF}_1^{\text{all}}$, and $\text{ARF}_2^{\text{all}}$ over oceanic area of 6 regions with high anthropogenic aerosol loading. The magnitudes of AOD and AOD_{anth} agree with those of *Chen et al.* (2011). $\text{ARF}_2^{\text{all}}$ values are overestimated by 1.5 W m^{-2} for mid-latitude regions (e.g., East Asia and Eastern U.S.), while those are underestimated by 0.7 W m^{-2} for low-latitude regions (e.g., India, Southeast Asia, and Australia) compared with $\text{ARF}_1^{\text{all}}$ values. As a whole, the globally averaged magnitude of $\text{ARF}_2^{\text{all}}$ is

positively increased throughout the year, and the seasonal variation is larger than that for ARF_1^{all} . Meanwhile, the sign of ARF_2^{all} shows seasonal discrepancy in each region. The sign is consistently positive over East Asia and Eastern U.S. with more than 0.8 of cloud fraction, while it is negative over Southeast Asia during whole seasons. For the India and Australia ARF_2^{all} is negative during other seasons except for summer.

Table 5.3. Regionally and globally averaged aerosol optical depth for total aerosols (AOD) and anthropogenic aerosols (AOD_{anth}), aerosol radiative forcing for all-sky by Chen et al. (2011) (ARF_1^{all}), and the present study (ARF_2^{all}) for four seasons of the year 2005.

Regions	Location		MAM		JJA		SON		DJF	
	Longitude (°)	Latitude (°)	AOD/ AOD*		AOD/ AOD*		AOD/ AOD*		AOD/ AOD*	
East Asia	100°E–150°E	20N°–50°N	0.34/ 0.15	–1.32/ 0.58	0.31/ 0.23	–1.60/ 1.78	0.22/ 0.11	–1.23/ 0.83	0.18/ 0.07	–0.70/ 1.33
India	60°E–100°E	0°–30°N	0.27/ 0.10	–2.41/ –2.62	0.37/ 0.08	–0.12/ 0.17	0.22/ 0.08	–0.21/ –2.28	0.20/ 0.09	–3.38/ –3.57
Southeast Asia	100°E–130°E	0°–20°N	0.28/ 0.15	–2.98/ –2.75	0.22/ 0.11	–1.95/ –1.63	0.22/ 0.10	–1.58/ –1.12	0.22/ 0.08	–1.78/ –1.64
Australia	100°E–150°E	20°S–0°	0.13/ 0.06	–1.06/ –0.58	0.13/ 0.07	–1.58/ –1.25	0.18/ 0.06	–1.17/ –1.30	0.15/ 0.05	–0.53/ –0.62
Eastern U. S.	80°W–50°W	25°N–45°N	0.19/ 0.08	–0.70/ 0.83	0.19/ 0.13	–0.86/ 0.82	0.12/ 0.04	–0.47/ 0.48	0.10/ 0.02	–0.13/ 0.45
Global	0°–360°	60°S–60°N	0.15/ 0.05	–0.46/ –0.30	0.16/ 0.08	–0.42/ 0.43	0.15/ 0.06	–0.47/ –0.17	0.12/ 0.03	–0.33/ –0.15

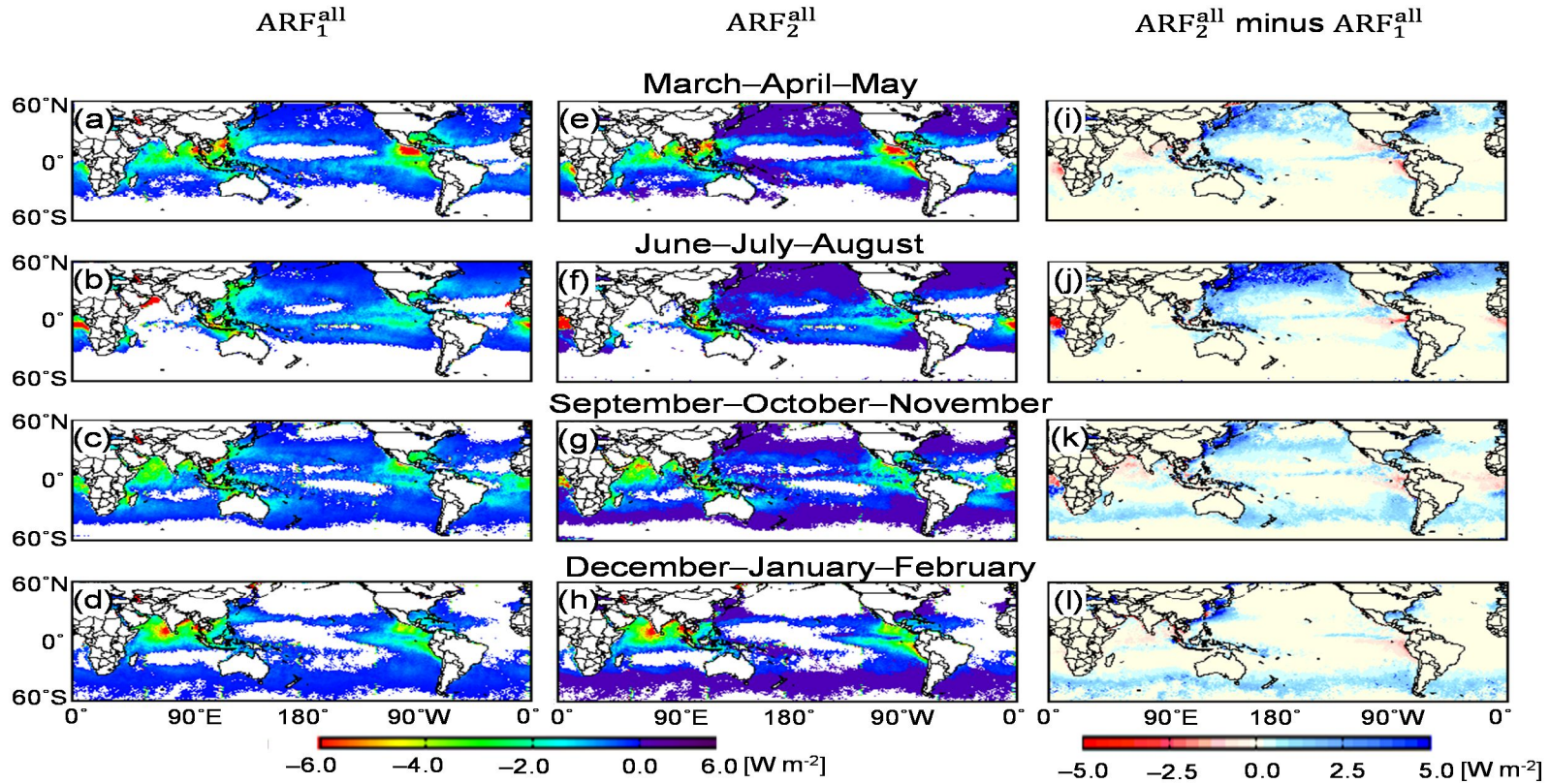


Figure 5.9. Global distribution of anthropogenic aerosol radiative forcing (ARF) for all-sky by Chen et al. (2011) (ARF_1^{all} ; a–d) and the present study (ARF_2^{all} ; e–h) and their difference (i–l) for four seasons of the year 2005.

5.2.3 Validation and assessment of its uncertainty

Since the RTM-simulated ΔDRE is applied to estimate aerosol DRE^{all} , the validation of the ΔDRE (in Fig. 5.4) is accomplished by TOA fluxes, clouds, and aerosols from the CERES. To test this relation between COD and ΔDRE , three regions with heavy aerosol loading were selected. The geographic coordinates and the mean aerosol optical properties obtained from the CERES for the three regions are given in Table 5.4 and the aerosol properties were used for calculating the ΔDRE from the RTM. To validate the ΔDRE , the observed shortwave flux for all-sky scenes was employed from the CERES. In this observed flux, two important contributions are included; namely, the cloud radiative effect and aerosol contribution for all-sky scenes. And the aerosol influence for all-sky can be divided into aerosol DRE^{clear} and ΔDRE , again. Therefore, to derive ΔDRE from observations, the cloud radiative effect and DRE^{clear} should be decoupled. The both cloud radiative effect and aerosol DRE^{clear} were simulated using the RTM and subtracted from the observed shortwave flux for all-sky condition of the real atmosphere.

The results are shown in Fig. 5.4. The ΔDRE s, both observed (box plots) and simulated (black dots), increased with increasing COD. This indicates that clouds contribute to weaken the cooling effect of aerosols (*Liao and Seinfeld, 1998*). Regional discrepancies in ΔDRE s exist, and among the three regions, ΔDRE over China (Fig. 5.4a) was distinguishable from the others. The median and ranges of ΔDRE s over China were larger than those over India and Africa.

These regional discrepancies may originate from the aerosol optical properties in Table 5.3. Aerosols over China have relatively lower ASSA and AAF, but a higher AOD. *Podgorny and Ramanathan* (2001) and *Keil and Haywood* (2003) pointed out that an absorbing aerosol, such as soot and black carbon particles, enhances the radiative warming at the TOA under cloudy-sky conditions.

There are also the differences between the simulated and observed Δ DRE. Compared with the mean value of the observed Δ DRE for each bin of COD, the simulation seems to underestimate the Δ DRE for a relatively small COD, but overestimate the Δ DRE for a large COD over all regions. The large differences observed for optically thin cloud (< 5) may have been due to inaccurate detection of cirrus clouds from the observation. Moreover, the observed Δ DREs had a negatively skewed wide range for all regions. As to the disparity between the observation and simulated results, a potential reason has been proposed. Above all, the use of the bulk values, averaged regionally in Table 5.4, could have led to this difference. Also, as shown from the simulation, the Δ DRE was induced solely by clouds, but that from the observation was also influenced by many factors (e.g., aerosol semi- and indirect effect) other than clouds.

There are several uncertainties associated with our estimation of aerosol DRE for all-sky, the induced uncertainties from the following sources are given in Table 5.4. The source of uncertainty is classified into two subjects. One is induced by retrieval error of inputted parameters, the other is associated cloud. Among input parameters, the first source of uncertainty is from AOD over land

and ocean. *Remer et al.* (2005) expected that the uncertainty of AOD over land and ocean is $0.05 \pm 0.15 \times \text{AOD}$ and $0.03 \pm 0.05 \times \text{AOD}$, respectively. Considering the uncertainty by AOD, it can cause about 8.3% uncertainty in aerosol DRE for all-sky. The second error source is the uncertainty associated with the estimation of ASSA and AAF discussed in section 4.1.2. In the study, we derived ASSA and AAF based on the CERES fluxes and AOD. Therefore, there is a measurement error due to high surface albedo in high latitude, and a conversion error from CERES radiances to fluxes, which contributes to the uncertainty of ± 0.03 (± 0.05) for ASSA (AAF). The overall uncertainty associated with ASSA and AAF is about 28.6% and 25.7% of the total aerosol DRE for all-sky, which is the largest influencing factor among the several error sources. The third is the error related to various cloud properties. Along with AOD, these cloud properties also have a retrieval uncertainty within a range of 15% of each property. Aerosol DRE for all-sky can be affected by 20% with respect to cloud property. Namely, considering increase in cloud mask of 15% over the globe, aerosol DRE for all-sky also increases in 28.6%.

Besides various input parameters related to aerosol and cloud, cloud and aerosol vertical profile can be one another error source in aerosol DRE for all-sky. Therefore, we performed the associated sensitivity to examine the influence by a vertical distribution of aerosol and cloud. In the test, five vertical distributions of aerosol are assumed (Fig. 5.5a). In the simulation, the cloud layer is fixed at 2 km and other conditions are equal to that for ΔDRE in Fig. 3. Profile 1 is of

aerosol below cloud and profile 2 is of aerosol in cloud, and the other profiles are of aerosol above cloud. Fig. 5.5b shows the dependence of ΔDRE on COD for $ASSA=0.96$ and $AAF=0.70$ for the five aerosol profiles. Overall, the increasing pattern of ΔDRE with respect to COD is similar for the all cases. Also, ΔDRE for equal COD is large when aerosols exist in high altitude. We note that ΔDRE is different for profiles 1, 2, and 3, while not for profile 3, 4, and 5. This implies that ΔDRE is not subject to when aerosol is above cloud.

Table 5.4. ΔDRE as a function of global COD from CERES observation (box plots) and RT model (solid circles). The box plots sum up the distribution, median, and variability of ΔDRE .

	Longitude (°)	Latitude (°)	CERES parameters	observed	Estimated parameters	
			Solar zenith angle (°)	Surface albedo	ASSA	AAF
China	100°E– 130°E	20°N– 45°N	40.7°	0.15	0.93	0.67
India	70°E–95°E	10°N– 30°N	33.0°	0.13	0.93	0.71
Africa	5°W–30°W	10°N– 30°N	33.0°	0.15	0.95	0.71

Table 5.5. Error sources in DRE for all-sky and its uncertainty.

Source of uncertainty		Extent	Reference	Uncertainty in DRE _{all} (%)
Model error source	Difference in shortwave fluxes from between RTM and CERES	10% of DRE ^{clear}	Oh et al. (2013)	7.6
Retrieval error source	MODIS AOD	0.05±0.15τ in land 0.03±0.05τ in ocean	Remer et al. (2005)	30.5, 22.9*, 30.9**
	Aerosol single scattering albedo	±0.03	Choi et al. (2009)	11.5
	Aerosol asymmetry factor	±0.05	Choi et al. (2009)	24.2
	MODIS cloud mask	15%	Ackerman et al. (2008)	17.9
	MODIS cloud optical depth	8%	Dong et al. (2008)	8.4
	MODIS cloud effective radius	15%	Dong et al. (2008)	0.03
	MODIS cloud top temperature	1K	Dong et al. (2008)	0.9
	Surface albedo	10%	Jin et al. (2003)	4.1
	Aerosol above cloud	20.33% of the total case	Table 4 in this study	15.7
	Relative altitude of aerosol and cloud			

* This value is for land.

** This value is for ocean.

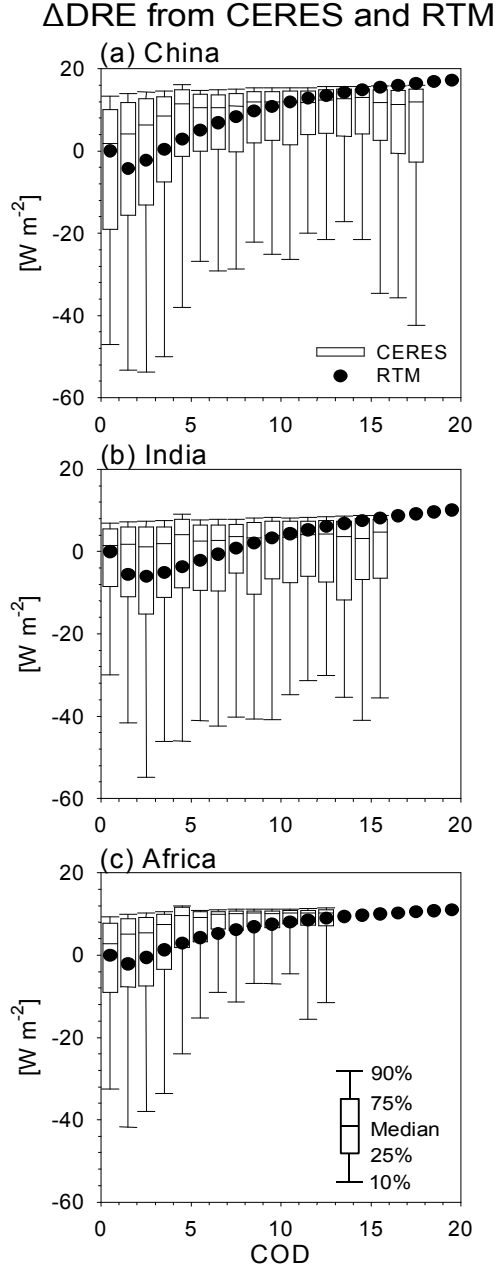


Figure 5.10. Dependency in the ΔDRE as a function of the COD for (a) south east China (100°E – 130°E , 20°N – 45°N), (b) India (70°E – 95°E , 10°N – 30°N) and (c) Africa (5°W – 30°W , 10°N – 30°N) from the CERES-observation and RT model. The box plots are the CERES observations, which sum up the distribution, median and variability in the ΔDRE corresponding to the COD. The solid circles are the ΔDRE simulated by the RT model over each region.

5.3. *Summary and discussions*

By considering the influence of clouds on aerosol DRE, this study has estimated aerosol DRE for both cloudy and cloud-free scenes. In this study we attempted to circumvent conventional limitation of the aerosol DRE estimations for cloudy scenes based on satellite observations which are confined to cloud-free scenes. Our method uses shortwave flux, surface albedo, aerosol from CERES, and cloud properties from MODIS. Our method using monthly satellite observations and RTM is a fast and cost-efficient way to determine monthly varying aerosol radiative effects, and is distinguished from previous methods using chemical transport models. The results provided the consistent evidence that clouds can suppress or enhance direct radiative cooling by aerosols, which also depends on aerosol optical properties and surface albedo (Figure 5.11). On the basis of our calculation, the average \pm standard deviation of DRE^{all} is -3.5 ± 2.3 (-3.1 ± 1.0) $W\ m^{-2}$ over the East Asia ($60^{\circ}S-60^{\circ}N$), which is approximately one third of the DRE for cloud-free scenes (-9.3 ± 2.1 $W\ m^{-2}$ over East Asia, -7.3 ± 1.6 $W\ m^{-2}$ over $60^{\circ}S-60^{\circ}N$). The value of DRE^{all} minus DRE^{clear} is positive for all oceanic regions but can be negative for land regions with high surface albedos. Particularly for $30^{\circ}S-60^{\circ}S$, the aerosol radiative cooling was largely canceled out. In addition, the monthly variation in DRE^{all} in this region differed significantly from that of DRE^{clear} , implying that cloud variation can alter the time variation in DRE.

Because of the observational limitations in satellite remote sensing, modeling studies have been performed by using climate and chemical models to globally estimate DRE^{all} , which improved our understanding of the influence of clouds on the DRE. Nevertheless, imperfect parameterizations in these models induce a large uncertainty in quantification of the all-sky DRE, and its near-real-time estimation is currently impossible owing to the heavy computing demand. However, this study has straightforwardly estimated all-sky DRE by using satellite observations to the fullest capacity with the aid of the pre-calculated look-up table from RTM. This methodology is more likely to be a satellite remote sensing technique commonly used to retrieve level-2 products. The key for this methodology was the observational extraction of aerosol optical properties, ASSA and AAF, which enabled calculation of a reliable DRE for all-sky scenes.

On the global average all-sky aerosol DRE values are -2.0 W m^{-2} in Loeb and Manalo-Smith (2005), -3.0 W m^{-2} in Kim and Ramanathan (2008), -2.9 W m^{-2} in Zhao et al. (2011), -1.0 W m^{-2} in Chen et al. (2011) (for anthropogenic aerosol only), and -3.1 W m^{-2} in the present study. These estimates were obtained by different methods, but are fairly comparable with our result. All is lower than clear-sky DREs (about -5.0 W m^{-2} in the global average) summarized in IPCC AR4 (2007), consistently supporting that aerosol DREs generally weakened once cloud effects were considered. However, caution must be exercised in interpreting the results because of various error sources. For this

reason, further studies should be performed to reduce a retrieval uncertainty with more reliable observations.

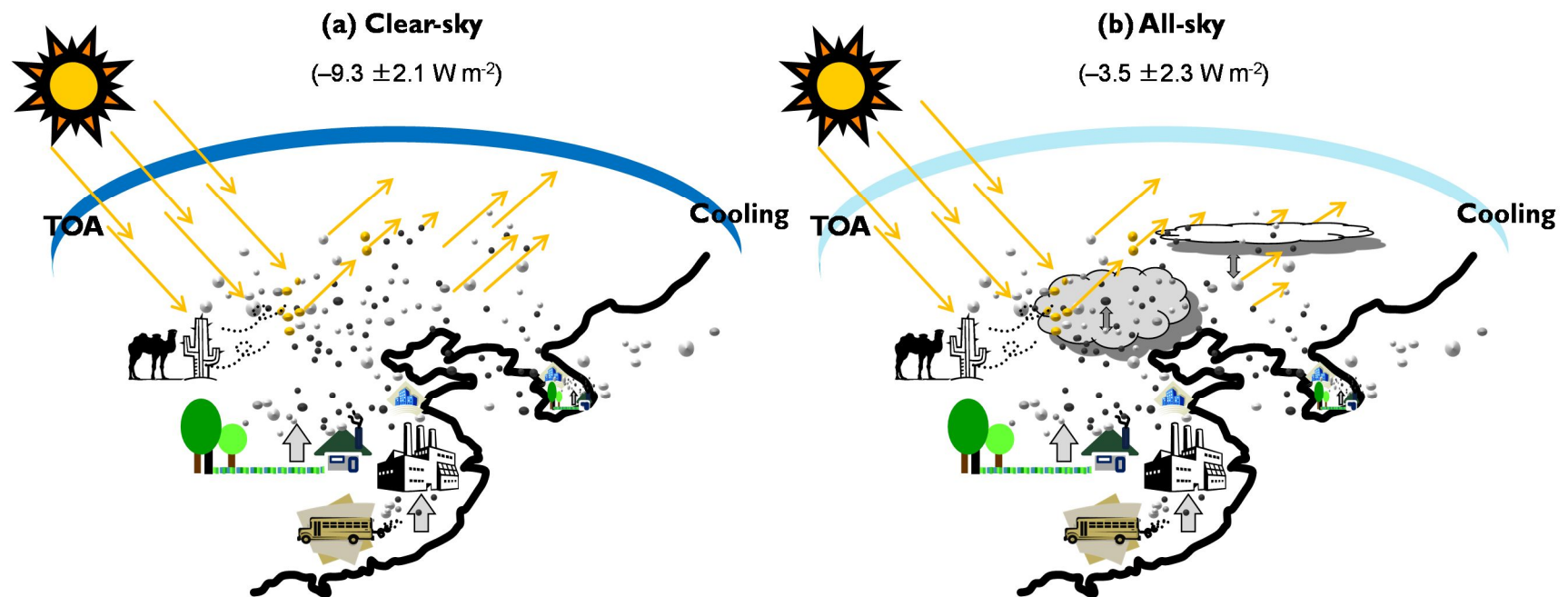


Figure 5.11. Summary of aerosol radiative effect for clear-sky (a) and all-sky (b) over East Asia.

6. GENERAL CONCLUSIONS

In the thesis, we try to reveal the mechanism of occurrence and transport for the multi-day high-PM₁₀ episodes in Seoul, Korea and its link with air pollutants originating in China and further diagnosis and assessment of climatic radiative impact of total and anthropogenic aerosol for all-sky over East Asia.

Based on several observational analyses, we established that the atmospheric fields over China and its neighboring countries may determine the amount of air pollutants transported from eastern China into Seoul, and thus the duration of high-PM₁₀ episodes in Seoul. Compared to 1-day episodes, Seoul was found to be strongly affected by massive air pollutions over eastern China in the early stage of a multi-day high-PM₁₀ episode. In this study, due to the lack of emission quantity data in Seoul, it was difficult to quantify the level of contribution from local emissions. Nevertheless, when it is taken account that the episodes occur under the very strong anomalous high-pressure system and the weak zonal wind in Seoul, it is suspected that local emissions may also cause further deterioration in the air quality within the city.

By considering the influence of clouds on the aerosol DRE, this study estimated the aerosol DRE^{all} over East Asia using shortwave flux, surface albedo, aerosol from the CERES and cloud properties from the MODIS. The CERES/MODIS observations combined with RT modeling provided evidence that clouds can suppress or enhance the direct radiative cooling by aerosols, which depends on the aerosol optical properties and surface albedo. The average

\pm standard deviation of aerosol DRE for all skies was $-3.5 \pm 2.3 \text{ W m}^{-2}$ over the globe, which is approximately one third of that for the clear skies ($-9.3 \pm 2.1 \text{ W m}^{-2}$). The difference between the $\text{DRE}^{\text{clear}}$ and DRE^{all} was positive for all ocean regions, but can be negative for some land regions with a high surface albedo.

So far, only the clear sky DRE of aerosols has been observed from satellites, but not that for an all-sky. Due to the observational limitations, modeling studies have been performed using climate and chemical models to globally estimate the DRE^{all} , which gives a better understanding of the influence of clouds on the aerosol DRE. Nevertheless, these models contain large uncertainty in quantification of the all-sky DRE. However, this study has straightforwardly estimated the aerosol DRE using satellite observations and RTM. The key for this was the observational extraction of the ASSA and AAF, which enabled a reliable DRE for all-sky scenes to be obtained.

The *IPCC* (2007) summarized various studies on aerosol DREs at the TOA for a clear sky: the global means from satellite remote sensing and modeling were about -5.4 and -3.0 W m^{-2} , respectively. Meanwhile, the aerosol DRE for all-sky scenes was somewhat different from that for clear-sky scenes: the globally averaged value was -3.0 W m^{-2} in the present study, -2.0 W m^{-2} in Loeb and *Manalo-Smith* (2005), -3.0 W m^{-2} in *Kim and Ramanathan* (2008), and -2.9 W m^{-2} in *Zhao et al.* (2011). Consistently, these studies estimated weaker aerosol DREs after applying cloud correction.

The present study demonstrated a possible regulation effect of clouds on aerosol radiative cooling effect. Yet we must be cautious to interpret the results because we used prescribed aerosol vertical profiles, which leads to about 12.1% of uncertainty in aerosol DRE^{all} . Also, among various error sources associated with aerosol and cloud, the ASSA and AAF over bright surfaces and for high latitudes may be inaccurate, and can cause 28.6 and 25.7% of appreciable uncertainties in DRE^{all} , respectively. For those regions, the further studies should carry out validation of ASSA and AAF values with more detailed observations and examine DRE^{all} with vertical profiles obtained from the CALIOP observation.

This thesis tries to understand the aerosol-cloud interaction on the radiative process and to reliably quantify these impacts on the energy budget based on the space-borne observation on the regional and global scale. These efforts in the study contribute to reduce the large uncertainty by aerosols reported in *IPCC* (2007), which can evaluate more accurate aerosol direct impact further indirect effect and give some insight to simulate the future climate in model.

REFERENCE

- Ackerman, S. A., R. E. Holz, R. Frey, E. W. Eloranta, B. C. Maddux, and M. McGill, 2008, Cloud detection with MODIS. Part II: Validation, *J. Atmos. Oceanic Technol.*, 25, 1073–1086.
- Anderson, T., Y. Wu, D. A. Chu, B. Schmid, J. Redemann, and O. Dubovik, 2005, Testing the MODIS satellite retrieval of aerosol fine-mode fraction, *J. Geophys. Res.*, 110, doi:10.1029/2005JD005978.
- Andrews, E., et al., 2006, Comparison of methods for deriving aerosol asymmetry parameter, *J. Geophys. Res.*, 111, doi:10.1029/2004JD005734.
- Annez, P. C., and R. M. Buckley, 2009, Urbanization and growth: setting the context, *Urbanization and growth*.
- Bates, T. S., et al., 2006, Aerosol direct radiative effects over the northwest Atlantic, northwest Pacific, and North Indian Oceans: Estimates based on in-situ chemical and optical measurements and chemical transport modeling, *Atmos. Chem. Phys.*, 6, 1657–1732.
- Bellouin, N., O. Boucher, J. Haywood, and M. S. Reddy, 2005, Global estimate of aerosol direct radiative forcing from satellite measurements, *Nature*, 438, 1138–1141.
- Berk, A., L. W. Bernstein, and D. C. Robertson, 1983, MODTRAN: A moderate resolution model for LOWTRAN7, *Rep. AFGL-TR-83-0187*, 261.

- Chand, D., T. L. Anderson, R. Wood, R. J. Charlson, Y. Hu, Z. Liu, and M. Vaughan, 2008, Quantifying above-cloud aerosol using spaceborne lidar for improved understanding of cloudy-sky direct climate forcing, *J. Geophys. Res.*, 113, doi:10.1029/2007JD009433.
- Chand, D., R. Wood, T. L. Anderson, S. K. Satheesh, and R. J. Charlson, 2009, Satellite-derived direct radiative effect of aerosols dependent on cloud cover, *Nat. Geosci.*, 2, 181–184.
- Charlock, T. P., F. G. Rose, D. A. Rutan, L. H. Coleman, T. Caldwell, and S. Zentz, 2005, Global, multi-year analysis of clouds and Earth's radiant energy system Terra observations and radiative transfer calculations, *15th ARM science team meeting*, Daytona Beach, Florida. [Available online at <http://www-cave.larc.nasa.gov/cave/pdfs/Charlock.15ARM05.pdf>]
- Clarke A., and V. Kapustin, 2010, Hemispheric aerosol vertical profiles: Anthropogenic impact on optical depth and cloud nuclei, *Science*, 329, 1488-1492.
- Chen, B., and H. Kan, 2008, Air pollution and population health: a global challenge, *Environ. Health Prev. Med.*, 13(2), 94–101.
- Chen, L., G. Y. Shi, S. G. Qin, S. Yang, and P. Zhang, 2011, Direct radiative forcing of anthropogenic aerosols over oceans from satellite observations, *Adv. Atmos. Sci.*, 28, 973–984, doi:10.1007/s00376-010-9210-4.
- Chin, M., P. Ginoux, S. Kinne, O. Torres, B. N. Holben, B. N. Duncan, R. V. Martin, J. A. Logan, A. Higurashi, and T. Nakajima, 2002, Tropospheric

- aerosol optical thickness from the GOCART model and comparisons with satellite and sunphotometer measurements, *J. Atmos. Sci.*, 59, 461–483.
- Choi, Y.-S., C.-H. Ho, M. H. Ahn, and Y. M. Kim, 2007, An exploratory study of cloud remote sensing capabilities of the Communication, Ocean and Meteorological Satellite (COMS) imagery, *Int. J. Remote. Sens.*, 28, 4715–4732.
- Choi, Y.-S., and C.-H. Ho, 2009a, Validation of the cloud property retrievals from the MTSAT-1R imagery using MODIS observations, *Int. J. Remote. Sens.*, 30, 5935–5958.
- Choi, Y.-S., C.-H. Ho, H.-R. Oh, R. Park, and C. G. Song, 2009b, Estimating bulk optical properties of aerosols over the western North Pacific by using MODIS and CERES measurements, *Atmos. Environ.*, 43, 5654–5660.
- Christopher, S. A., and J. L. Zhang, 2004, Cloud-free shortwave aerosol radiative effect over oceans: Strategies for identifying anthropogenic forcing from Terra satellite measurements, *Geophys. Res. Lett.*, 31, doi:10.1029/2004GL020510.
- Devasthale, A., and M. A. Thomas, 2011, A global survey of aerosol-liquid water cloud overlap based on four years of CALIPSO-CALIOP data, *Atmos. Chem. Phys.*, 11, 1143–1154.
- Di Iorio, T., A. di Sarra, D. M. Sferlazzo, M. Cacciani, D. Meloni, F. Monteleone, D. Fuà, and G. Fiocco, 2009, Seasonal evolution of the

- tropospheric aerosol vertical profile in the central Mediterranean and role of desert dust, *J. Geophys. Res.*, 114, D02201, doi:10.1029/2008JD010593.
- Dong, X., P. Minnis, B. Xi, S. Sun-Mack, and Y. Chen, 2008, Comparison of CERES-MODIS stratus cloud properties with ground-based measurements at the DOE ARM Southern Great Plains site, *J. Geophys. Res.*, 113, doi: 10.1029/2007JD008438.
- Draxler, R., and G. Rolph, 2013, HYSPLIT (HYbrid Single-Particle Lagrangian Integrated Trajectory) Model access via NOAA ARL READY. NOAA Air Resources Laboratory: Silver Spring, MD, Available at <http://ready.arl.noaa.gov/HYSPLIT.php>.
- Dubovik, O., B. N. Holben, T. F. Eck, A. Smirnov, Y. J. Kaufman, M. D. King, D. Tanré, and I. Slutsker, Variability of absorption and optical properties of key aerosol types observed in worldwide locations, 2002, *J. Atmos. Sci.* 59, 590–608.
- Eck, T. F., B. N. Holben, O. Dubovik, A. Smirnov, I. Slutsker, J. M. Lobert, and V. Ramanathan, 2006, Column-integrated aerosol optical properties over the Maldives during the northeast monsoon for 1998–2000, *J. Geophys. Res.*, 106, 28,555–28,566.
- Fajersztajn, L., M., Veras, L. V. Barrozo, and P. Saldiva, 2013, Air pollution: a potentially modifiable risk factor for lung cancer, *Nat. Rev. Cancer*, 13(9), 674-678.

- Fu, Q., and K. N. Liou, 1993, Parameterization of the radiative properties of cirrus clouds, *J. Atmos. Sci.*, 50, 2008–2025.
- Fu, X., S. X. Wang, Z., Cheng, J. Xing, B. Zhao, J. D, Wang, and J. M. Hao, 2014, Source, transport and impacts of a heavy dust event in the Yangtze River Delta, China in 2011, *Atmos. Chem. Phys.*, 14, 1239–1254.
- Haywood, J. M., V. Ramaswamy, and B. J. Soden, 1999, Tropospheric aerosol climate forcing in clear-sky satellite observations over the oceans, *Science*, 283, 1299–1303.
- Holz, R. E., S. A. Ackerman, F. W. Nagle, R. Frey, S. Dutcher, R. E. Kuehn, M. A. Vaughan, and B. Baum, 2008, Global Moderate Resolution Imaging Spectroradiometer (MODIS) cloud detection and height evaluation using CALIOP, *J. Geophys. Res.*, 114, doi: 10.1029/2008JD009837.
- Hu, Y., et al., 2009, CALIPSO/CALIOP cloud phase discrimination algorithm, *J. Atmos. Oceanic Technol.*, 26, 2293–2309.
- Intergovernmental Panel on Climate Change, 2007, *Climate Change 2007: The Physical Science Basis*, Cambridge University Press.
- Jung, C. H., Y. S. Cho, S. M. Hwang, Y. G. Jung, J. C. Ryu, and D. S. Shin, 2007, Analysis of measurement error for PM-10 mass concentration by inter-comparison study, *J. Korean Soc. Atmos. Environ.*, 23, 689–698.
- Kalnay, E., et al., 1996, The NCEP/NCAR 40-year reanalysis project, *Bull. Amer. Meteor. Soc.*, 77(3), 437–471.

- Kaufman, Y. J., O. Boucher, D. Tanre', M. Chin, L. A. Remer, and T. Takemura, 2005, Aerosol anthropogenic component estimated from satellite data, *Geophys. Res. Lett.*, 32, L17804, doi:10.1029/2005GL023125.
- Kaufman, Y. J., D. Tanre', and O. Boucher, 2002, A satellite view of aerosols in the climate system, *Nature*, 419, 215–223.
- Keil, A., and J. M. Haywood, 2003, Solar radiative forcing by biomass burning aerosol particles during SAFARI 2000: A case study based on measured aerosol and cloud properties, *J. Geophys. Res.*, 108, doi:10.1029/2002JD002315.
- Kim, D. Y., and V. Ramanathan, 2008, Solar radiation budget and radiative forcing due to aerosols and clouds, *J. Geophys. Res.*, 113, doi:10.1029/2007JD008434.
- King, M. D., S. C. Tsay, S. E. Plantnick, M. Wang, and K. N. Liou, 1997, Cloud retrieval algorithms for MODIS, MODIS algorithm theoretical basis document, NASA.
- Kneizys, F. X., E. P. Shettle, W. O. Gallery, J. H. Chetwynd, L. W. Abreu, J. E. A. Selby, S. A. Clough, and R. W. Fenn, 1983, Atmospheric transmittance/radiance: Computer code LOWTRAN 6, *Rep. AFGL-TR-83-0187*, 200p.
- Lee, S., C.-H. Ho, and Y.-S. Choi, 2011, High-PM₁₀ concentration episodes in Seoul, Korea: Background sources and related meteorological conditions, *Atmos. Environ.*, 45(39), 7240–7247.

- Lee, S., C.-H. Ho, Y.-G. Lee, H.-J. Choi, and C.-K. Song, 2013, Influence of transboundary air pollutants from China on the high-PM₁₀ episode in Seoul, Korea for the period October 16–20, 2008, *Atmos. Environ.*, 77, 430–439.
- Levy, R. C., L. A. Remmer, D. Tanré, Y. J. Kaufman, C. Ichoku, B. N. Holben, J. M. Livingston, P. B. Russell, and H. Maring, 2003, Evaluation of the Moderate-Resolution Imaging Spectroradiometer (MODIS) retrievals of dust aerosol over the ocean during PRIDE, *J. Geophys. Res.*, 108, doi:10.1029/2002JD002460.
- Liao, H., and J. H. Seinfeld, 1998, Effect of clouds on direct aerosol radiative forcing of climate, *J. Geophys. Res.*, 103, 3781–3788.
- Lin, J. et al., 2014, China's international trade and air pollution in the United States, *Proc. Nati. Acad. Sci.*, 201312860.
- Loeb, N. G., and N. Manalo-Smith, 2005, Top-of-atmosphere direct radiative effect of aerosols over global oceans from merged CERES and MODIS observations, *J. Clim.*, 18, 3506–3526.
- McClatchey, R. A., R. W. Fenn, and J. E. A. Selby, F. E. Volz, and J. S. Garing, 1972, Optical properties of the atmosphere. (3rd ed.), *AFCRL Environ. Res. Pap.* 411, 108p.
- McComiskey, A., S. E. Schwartz, B. Schmid, H. Guan, E. R. Lewies, P. Ricchiazzi, and J. A. Ogren, 2008, Direct aerosol forcing: Calculation

- from observables and sensitivities to inputs, *J. Geophys. Res.*, 113, doi: 10.1029/2007JD009170.
- Menzel, W. P., W. L. Smith, and T. R. Stewart, 1983, Improved Cloud Motion Wind Vector and Altitude Assignment Using Vas, *J. Appl. Meteorol.*, 22, 377–384.
- Omar, et al., 2009, The CALIPSO automated aerosol classification and lidar ratio selection algorithm, *J. Atmos. Oceanic Technol.*, 26, 1994–2014.
- Oreopoulos, L., and S. Platnick, 2008, Radiative susceptibility of cloudy atmospheres to droplet number perturbations: 2. Global analysis from MODIS, *J. Geophys. Res.*, 113, doi:10.1029/2007JD009655.
- Pant P., P. Hegd, U. C. Dumka, R. Sagar, S. K. Satheesh, K. K. Moorthy, A. Saha, and M. K. Srivastava, 2006, Aerosol characteristics at a high-altitude location in central Himalayas: Optical properties and radiative forcing, *J. Geophys. Res.*, 111, doi: 10.1029/2005JD006768.
- Park, S. U., J. H. Cho, and M. S. Park, 2013, Analyses of high aerosol concentration events (dense haze/mist) occurred in East Asia during 10–16 January 2013 using the data simulated by the Aerosol Modeling System, *Int. J. Chem.*, 2(3), 10–26.
- Patadia, F., P. Gupta, and S. A. Christopher, 2008, First observational estimates of global clear sky shortwave aerosol direct radiative effect over land, *Geophys. Res. Lett.*, 35, doi 10.1029/2007GL032314.

- Platnick, S., M. D. King, S. A. Ackerman, W. P. Menzel, B. A. Baum, J. C. Riedi, and R. A. Frey, 2003, The MODIS cloud products: Algorithms and examples from Terra, *IEEE Trans. Geosci. Remote. Sens.*, 41, 459–473.
- Podgorny, I. A., and V. Ramanathan, 2001, A modeling study of the direct effect of aerosols over the tropical Indian Ocean, *J. Geophys. Res.*, 106, 24097–24105.
- Qu, W. J., R. Arimoto, X. Y. Zhang, C. H. Zhao, Y. Q. Wang, L. F. Sheng, and G. Fu, 2010, Spatial distribution and interannual variation of surface PM₁₀ concentrations over eighty-six Chinese cities, *Atmos. Chem. Phys.*, 10(12), 5641–5662.
- Quijano, A. L., I. N. Sokolik, and O. B. Toon, 2000, Influence of the aerosol vertical distribution on the retrievals of aerosol optical depth from satellite radiance measurements, *Geophys. Res. Lett.*, 27, 3457–3460.
- Ramanathan, V., P. J. Crutzen, J. T. Kiehl, and D. Rosenfeld, 2001, Atmosphere - Aerosols, climate, and the hydrological cycle, *Science*, 294, 2119–2124.
- Remer, L. A., D. Tanré, Y. J. Kaufman, C. Ichoku, S. Mattoo, R. Levy, D. A. Chu, B. Holben, O. Dubovik, A. Smimov, J. V. Martins, R. R. Li, and Z. Ahmad, 2002, Validation of MODIS aerosol retrieval over ocean, *Geophys. Res. Lett.*, 29, doi:10.1029/2001GL013204.
- Remer, L. A., et al., 2005, The MODIS aerosol algorithm, products, and validation, *J. Atmos. Sci.*, 62, 947–973.

- Remer, L. A., and Y. J. Kaufman, 2006, Aerosol direct radiative effect at the top of the atmosphere over cloud free ocean derived from four years of MODIS data, *Atmos. Chem. Phys.*, 6, 237–253.
- Ricchiazzi, P., S. R. Yang, C. Gautier, and D. Sowle, 1998, SBDART: A research and teaching software tool for plane-parallel radiative transfer in the Earth's atmosphere, *B. Am. Meteorol. Soc.*, 79, 2101–2114.
- Rossow, W. B., A.W. Walker, L. C. Garder, 1993, Comparison of ISCCP and other cloud amounts, *J. Clim.*, 6, 2394–2418.
- Rutan, D., F. Rose, M. Roman, N. Manalo-Smith, C. Schaaf, and T. Charlock, 2009, Development and assessment of broadband surface albedo from Clouds and the Earth's Radiant Energy System Clouds and Radiation Swath data product, *J. Geophys. Res.*, 114, doi 10.1029/2008jd010669.
- Shettle, E. P., and R. W. Fenn, 1975, Models for the aerosols of the lower atmosphere and the effects of humidity variations on their optical properties, *AFGL-TR-79-0214*, 94p.
- Takemura T., T. Nakajima, O. Dubovik, B. N. Holben, and S. Kinne, 2002, Single-scattering albedo and radiative forcing of various aerosol species with a global three-dimensional model, *J. Clim.*, 15, 333–352.
- Yu, H., M. Chin, L. A. Remer, R. G. Kleidman, N. Bellouin, H. Bian, and T. Diehl, 2009, Variability of marine aerosol fine-mode fraction and estimates of anthropogenic aerosol component over cloud-free oceans

- from the Moderate Resolution Imaging Spectroradiometer (MODIS), *J. Geophys. Res.*, 114, D10206, doi:10.1029/2008JD010648.
- Yu, H., et al., 2006, A review of measurement-based assessments of the aerosol direct radiative effect and forcing, *Atmos. Chem. Phys.*, 6, 613–666.
- Valero, F. P. J., et al., 2003, Absorption of solar radiation by the clear and cloudy atmosphere during the Atmospheric Radiation Measurement Enhanced Shortwave Experiments (ARESE) I and II: Observations and models, *J. Geophys. Res.*, 108, doi:10.1029/2001JD001384.
- Wang, K. C., Dickinson, R. E., Su, L., and K. E. Trenberth, 2012, Contrasting trends of mass and optical properties of aerosols over the Northern Hemisphere from 1992 to 2011, *Atmos. Chem. Phys.*, 12, 9387–9398.
- Wang, L. T., et al., 2014, The 2013 severe haze over the southern Hebei, China: model evaluation, source apportionment, and policy implications, *Atmos. Chem. Phys.*, 14, 3151–3173.
- Winker, D. M., W. H. Hunt, and M. J. McGill, 2007, Initial performance assessment of CALIOP, *Geophys. Res. Lett.*, 34, doi:10.1029/2007GL030135.
- Xia, X., H. Chen, P. Goloub, W. Zhang, B. Chatenet, and P. Wang, 2007, A compilation of aerosol optical properties and calculation of direct radiative forcing over an urban region in northern China, *J. Geophys. Res.*, 112, doi:10.1029/2006JD008119.

- Zhang, J. L., S. A. Christopher, L.A. Remer, and Y. J. Kaufman, 2005, Shortwave aerosol radiative forcing over cloud-free oceans from Terra: 1. Angular models for aerosols, *J. Geophys. Res.*, 110, doi:10.1029/2004JD005008.
- Zhang, X. Y. et al., 2003, Characterization of soil dust aerosol in China and its transport and distribution during 2001 ACE Asia: 1. Network observations, *J. Geophys. Res.*, 108.D9.
- Zhao, T. X.-P., N. G. Loeb, I. Laszlo, and M. Zhou, 2011, Global component aerosol direct radiative effect at the top of atmosphere, *Int. J. Remote. Sens.*, 32, 633–655.
- Zhou, M., H. Yu, R. E. Dickinson, O. Dubovik, and B. N. Holben, 2005, A normalized description of the direct effect of key aerosol types on solar radiation as estimated from Aerosol Robotic Network aerosols and Moderate Resolution Imaging Spectroradiometer albedos, *J. Geophys. Res.*, 110, doi:10.1029/2005JD005909.

국문초록

전 세계 어떤 지역보다 아시아 대륙은 다양한 종류의 에어로졸이 많이 존재하는 지역이다. 특히, 중국에서 발생한 다량의 에어로졸과 국경을 넘은 이동은 사람들의 건강에 직접적인 문제를 일으킬 뿐만 아니라 지역규모의 기후에 영향을 준다는 점에서 동아시아 전 나라의 주요 관심사가 되어왔다.

그러므로 본 연구에서는 2001년부터 2013년까지의 기간 동안 서울에서 수일간 지속된 미세먼지 고농도 현상 (일 평균 미세먼지 농도 $100 \mu\text{g m}^{-3}$ 이상)을 대상으로 다양한 관측 자료에 기반하여 장기간 지속된 고농도 현상 발생 및 이동과 관련한 메커니즘을 밝히고자 한다. 분석 결과, 우리나라 풍상 측에 위치한 중국에서 발생한 에어로졸이 서울에서 수일간 지속되었던 미세먼지 고농도 현상과 매우 밀접한 관련이 있는 것으로 나타났다. 즉, 수일간 지속된 미세먼지 고농도 현상은 중국 북동부와 우리나라에 매우 강한 고기압 편차가 있을 때 발생하는 것으로 나타났다. 이는 결과적으로 대기 경계층 내에 있는 오염 물질을 가두는 역할을 하게 되고, 정체된 대기 조건에 의해 중국으로부터 하층의 약한 서풍을 타고 오염물질이 우리나라를 비롯한 주변국으로 수송되는 것으로 추정된다. 수일간 지속되는 미세먼지 고농도 현상은 단기적으로는 그 지역에서의 대기질 저하를 가져오는 한편, 장기적으로 보면 그 지역의 복사 특성과 에너지 수지에 영향을 줄 수 있다.

이에 본 연구에서는 2001년부터 2005년까지의 동아시아 지역 ($80^{\circ}\text{ E}-200^{\circ}\text{ E}$, $20^{\circ}\text{ N}-60^{\circ}\text{ N}$)에서 구름의 영향이 고려된 경우 (clear- and cloudy-sky), 관측자료에 기반하여 대기상한에서의 에어로졸 직접복사효과를 기후학적 측면에서 정량화 하고자 하였다. 현실적으로 타당한 복사효과의 정량화를 위해 청천 (clear-sky)에서 관측한 복사량과 구름 낀 하늘 (cloudy-sky)을 가정하였을 때 복사전달모델을 통해 계산된 복사량을 조합하여 각 격자마다의 에어로졸 직접 복사효과를 산출하였다. 청천의 관측 복사량은 Earth's Radiant Energy System (CERES) 위성 자료를 사용하였고, 구름낀 하늘에서의 복사량 모의를 위한 복사전달 모델에 사용되는 에어로졸과 구름 관련 산출물은 TERRA 위성의 Moderate Resolution Imaging Spectroradiometer (MODIS) 자료를

사용하였다. 모의 결과, 구름의 영향을 고려하였을 때 동아시아 지역에서 에어로졸 직접복사 효과는 $-3.57 \pm 2.3 \text{ W m}^{-2}$ 이고, 청천에서의 복사효과와 비교하면 음의 복사효과가 상대적으로 약해진 것이다. 이는 실제 현실에서 구름은 에어로졸의 산란 효과를 막음으로써 복사효과를 감소시키는 역할을 하는 것을 의미한다. 특히, 이런 구름의 효과는 광학적으로 두껍고 운량이 많은 해양에서 매우 뚜렷하게 나타난다. 그 결과, 이런 지역은 에어로졸로 인한 음의 복사효과가 거의 상쇄되는 것으로 나타난다.

본 연구에서 논의한 한국 지역에서 수일간 지속된 PM₁₀ 고농도 현상의 발생 및 이동 메커니즘과 복사효과에 대한 결과들은 기후학적 측면에서 동아시아 지역 기후에 대한 이해도 향상과 지역기후 모델의 미래 기후 모수화 능력 향상 기여할 것이다. 그리고 더 나아가, 장거리 이동하는 대기오염물질의 예측성 향상 및 관련 국가들의 협력에 과학적 근거가 될 것이다.

주요어: 에어로졸 직접 복사효과, 구름 낀 하늘, 구름, 위성 자료,
장기간 지속되는 미세먼지 고농도, 월경성 대기오염물질

학번: 2008-30113